

---

Unterschrift Betreuer



TECHNISCHE  
UNIVERSITÄT  
WIEN  
Vienna University of Technology

## MASTERARBEIT

# Simulation of Diamond Micro-Optics and Characterisation of Fibre-Coupled Diamond Defects

Ausgeführt am Atominstitut  
der Technischen Universität Wien

unter der Anleitung von

**Prof. Dr. Jörg Schmiedmayer und Dr. Michael Trupke**

durch

**Sarah Reisenbauer**

Königsegg 17, 2851 Krumbach

May 13, 2014

---

# Abstract

At present many new application fields are emerging from nitrogen-vacancy centre research - be it in quantum information and communication technologies, in quantum metrology or even in life sciences. Most applications and experiments require the possibility of reliable high efficiency measurements of the nitrogen-vacancy centre fluorescence light. In order to achieve that in our experiment different types of lenses, for focusing the fluorescence light, were compared in simulations with the software 'Comsol Multiphysics' in the first part of this thesis. Subsequently, the chosen type of lens was improved in a numerical optimization. The second part of the thesis proceeds with the assembly of an experimental apparatus for direct fibre coupling of the nitrogen vacancy centre fluorescence light. We tested a method of assembly and conducted magnetometry measurements by means of optically detected magnetic resonance. In the future we are going to construct a similar setup with a coupled single nitrogen vacancy centre to use it as a qubit, as a single photon source and for the study of the nitrogen vacancy centre physics.

# Zusammenfassung

Gegenwärtig entstehen viele neue Anwendungsfelder aus der Stickstoff-Fehlstellen-Zentrumsforschung - sei es im Bereich der Quanteninformations- und Kommunikationstechnologien, in der Quantenmetrologie oder in den Biowissenschaften. Die meisten Anwendungen und Experimente benötigen die Möglichkeit einer verlässlichen und effizienten Messung des Fluoreszenzlichtes der Stickstoff-Fehlstellen-Zentren. Um das in unserem Experiment zu erreichen, wurden verschiedenen Arten von Linsen, zur Fokussierung des Fluoreszenzlichtes, in Simulationen mit der Software 'Comsol Multiphysics' im ersten Teil dieser Arbeit verglichen. Darauf folgend wurde der ausgewählte Linsentyp durch numerische Optimierung verbessert. Der zweite Teil dieser Arbeit beschäftigt sich mit der Konstruktion eines neuen Aufbaues für direktes Faserkoppeln des Fluoreszenzlichtes der Stickstoff-Fehlstellen-Zentren. Wir testeten Methoden des Aufbaues und führten Magnetometriemessungen mit Hilfe von optisch detektierter magnetischer Resonanz durch. Zukünftig werden wir einen ähnlichen Aufbau mit einem einzelnen gekoppelten Stickstoff-Fehlstellen-Zentrum konstruieren um das Zentrum als Qubit, als Einzelphotonenquelle und für die Erforschung der Stickstoff-Fehlstellen-Zentrumsphysik zu verwenden.

# Contents

<b>1. Introduction</b>	<b>1</b>
1.1. Outline of the Thesis . . . . .	2
<b>2. Properties of the Nitrogen Vacancy Centre</b>	<b>3</b>
2.1. Physics of NV Defect Centres in Diamond . . . . .	3
2.1.1. Diamond Environment, Creation and Structure . . . . .	3
2.1.2. Electronic Structure . . . . .	5
2.1.3. Optical Properties of NV Ensembles . . . . .	6
2.2. Optically Detected Magnetic Resonance Measurements . . . . .	7
2.2.1. Zero-Field and Zeeman Splitting . . . . .	8
<b>3. Collection Optics Optimisation</b>	<b>9</b>
3.1. Setup Outline . . . . .	9
3.1.1. Proposed Experimental Setup . . . . .	9
3.1.2. Coupling Efficiency without Lens . . . . .	10
3.1.3. Proposed Collection Optics . . . . .	12
3.2. Comsol Multiphysics Simulations . . . . .	14
3.2.1. Comsol Multiphysics Software . . . . .	14
3.2.2. Comsol Simulation Setup . . . . .	16
3.2.3. Simulation Results and Conclusions . . . . .	19
3.3. Collection Optics Optimisation . . . . .	24
3.3.1. Optimisation Program . . . . .	24
3.3.2. Derived Lens . . . . .	29
3.3.3. Outlook . . . . .	29

<b>4. Direct Fibre Coupling of NV Ensembles</b>	<b>32</b>
4.1. Experimental Apparatus . . . . .	32
4.1.1. Setup Design . . . . .	33
4.1.2. Lasers and Optical System . . . . .	33
4.1.3. Theoretical Collection Efficiencies . . . . .	36
4.1.4. Diamond Properties . . . . .	39
4.1.5. RF System and Coils . . . . .	40
4.1.6. Detection System and Data Aquisition . . . . .	41
4.1.7. Assembly Process . . . . .	42
4.2. Optically Detected Magnetic Resonance Experiments . . . . .	44
4.2.1. Green Laser Illumination . . . . .	44
4.2.2. Red Laser Illumination . . . . .	47
<b>5. Conclusions and Outlook</b>	<b>54</b>
<b>A. Appendix</b>	<b>56</b>
A.1. Optimisation Program Source Code . . . . .	56

# 1. Introduction

Gems in a gem - single nitrogen vacancy (NV) centres in diamond comprise a very promising system for many near future high-tech applications. The first negatively charged single centre was detected in 1997 [1], some decades after extensive NV research had started. At that time, it became obvious that the NV<sup>-</sup> centre was suitable for stable single photon generation [2] and electronic spin state could be read out relatively easily [3], qualifying the centre as a possible solid state qubit for quantum information applications. Additionally, the centre shows long coherence times even at room temperature [3]. Some more applications have already been demonstrated: the use of the centre as sensor for magnetic fields, electric fields and temperature, which can be transferred into biological environments, for example a living cell [4]. In combination with nuclear spins room temperature quantum registers are within reach [5]. There have been proposals for quantum information systems that would permit good scalability [6].

The aim of the experiment in the team I could be part of is to couple multiple NV centres as qubits and quantum register together in a scalable quantum information system. Single NV centres will be directly coupled to a single mode fibre. Magnetic field and electric field strengths and orientations are going to be fully and individually adjustable and a microwave antenna for driving certain NV spin state transitions will be present. For enhancement of light coupling a collection micro-lens is inserted between the single mode fibre and the NV centre. This lens is created on the surface of the diamond by means of focused ion beam milling.

As an intermediate step to reach this goal we investigated the behaviour of different collection optics in simulations. The chosen type of lens was then further enhanced

by numerical means. Additionally, we constructed an experimental apparatus for direct fibre coupling of NVs and tested it with two different ensemble samples. In the course of assembly a second setup was developed and used for further measurements.

## **1.1. Outline of the Thesis**

A short introduction to the NV centre and its properties is given in chapter 2. The work on this thesis started with optical simulations of different lens types proposed for NV fluorescence light collection in the experiment. Determining their effectiveness was important for deciding on a specific type of lens in order to subsequently improve it for our requirements, as discussed in chapter 3. As second part of my work on the thesis, discussed in chapter 4, an experimental apparatus was built from scratch where NV ensembles were directly coupled to optical fibres without the use of confocal microscopy. Since the construction is work in progress, in chapter 5 an outlook for the future steps is given.

## 2. Properties of the Nitrogen Vacancy Centre

In this chapter some physical and theoretical background for the simulations and experiments discussed later in this thesis is presented. A short description of NV centres and their environment in diamond, as well as their electronic structure, the two charge states, the known energy levels and their transitions is given.

### 2.1. Physics of NV Defect Centres in Diamond

The NV centre is one of many different point defects common in diamond and consists of a nitrogen atom neighbouring a lattice vacancy. In nitrogen rich diamonds it exists naturally or can be created artificially [7].

#### 2.1.1. Diamond Environment, Creation and Structure

##### **Diamond**

As host material the properties of diamond are very important for the understanding of the physical behaviour of NV centres. Diamond consists of tetrahedrally ordered carbon atoms which form a face-centred cubic lattice with a dual basis. The second basis is displaced by one quarter of the space diagonal from the first one. The lattice constant is 0.3566 nm and nearest-neighbour distance is 0.1544 nm.

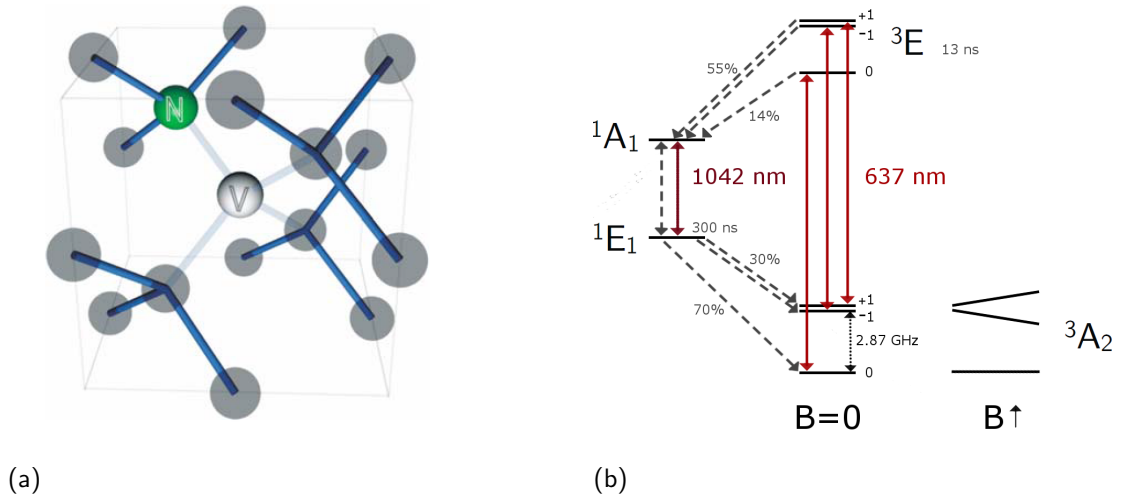


**Figure 2.1.:** (a) NV centre structure, where grey circles represent the diamond crystal carbon atoms [8]; (b) energy levels of  $NV^-$  at high temperature: continuous lines represent zero-phonon-line transitions, the dotted black line is a magnetic dipole transition and dotted grey lines are non radiative transitions. Important level lifetimes and decay channel probabilities are indicated as well as Zeeman splitting of the ground state levels.

Due to the high band gap of 5.5 eV diamond is a good electric insulator, it has high optical transparency as well as a high refractive index of about 2.4 [7].

### Physical Structure of NV-Centres

The nitrogen atom, which replaces a carbon atom of the diamond crystal, and the vacancy of the centre are oriented along the [111]-crystalline direction as illustrated in figure 2.1(a). Due to that there exist four crystallographically equivalent orientations of the centre [9]. The nitrogen atom is bound to the three surrounding carbon atoms but has two dangling bonds. With the three additional dangling bonds of the carbon atoms surrounding the vacancy the NV centre has five electrons forming electronic orbitals. This state is called  $NV^0$ . It can acquire a further sixth electron supposedly from nearby nitrogen atoms [10], forming the negatively charged state  $NV^-$ .

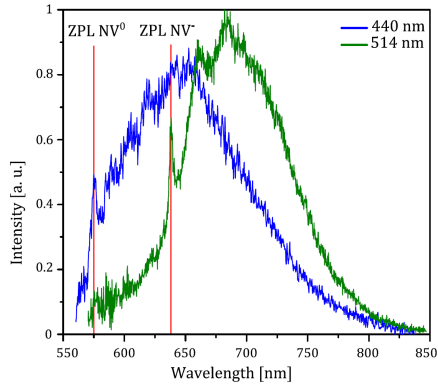
## Creation

NV centres exist naturally in diamond but can also be produced artificially in different ways. One method to produce NV centres in nitrogen rich diamond consists in producing vacancies by irradiation with neutrons, protons, electrons or various ions and subsequently annealing them at above 650 °C. The annealing process provides the necessary energy to make the vacancies mobile in the diamond to pair up with nitrogen atoms. It is also possible to implant nitrogen ions into diamond at precise locations [11].

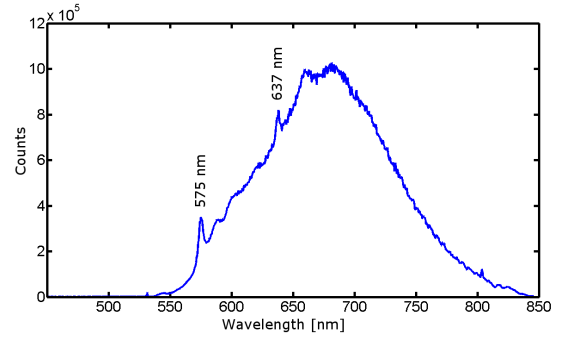
### 2.1.2. Electronic Structure

The electronic structures of  $NV^0$  and  $NV^-$  have been investigated in the last decades but are still under debate [12]. For this work the structure of  $NV^-$  is most important and therefore discussed more closely. Figure 2.1(b) illustrates the current state of knowledge of the  $NV^-$  energy levels that have been confirmed experimentally [13]. The ground state  $^3A_2$  of the centre is a spin triplet state with a zero magnetic field splitting (ZFS) in the  $m_s = 0$  and  $m_s = \pm 1$  sub levels of 2.87 GHz. At room temperature the excited state  $^3E$  behave as another spin triplet with ZFS of 1.42 GHz between the  $m_s = 0$  and  $m_s = \pm 1$  sub levels. The two singlet levels  $^1A_1$  and  $^1E_1$  are interjacent to the ground and excited states. The transitions from one state to another are coupled quite strongly to phonons so that there are only four optical dipole transitions not involving vibrational excitations called zero-phonon-lines (ZPL). Three are between  $^3A_2$  and  $^3E$  with a wavelength of 637 nm and one with a wavelength of 1042 nm from  $^1A_1$  to  $^1E_1$ . As shown in picture 2.1(b) there are magnetic dipole and non radiative transitions marked by dotted lines. Also lifetimes, spin and spin projection quantum numbers of the corresponding states are given.  $NV^0$  has a different term scheme, which is not relevant for this work, with a strong ZPL at 575 nm [9].

Room temperature fluorescence spectra of both centres (figure 2.2(a)) show a small peak at the ZPL wavelength when illuminated with higher energy light. Some



(a)



(b)

**Figure 2.2.:** (a) Spectra of  $NV^0$  and  $NV^-$  at room temperature for two different excitation energies [9]; (b) fluorescence spectrum of an NV ensemble with indicated ZPLs of  $NV^-$  and  $NV^0$  excited at 532 nm wavelength.

excitation energy is transferred to phonons, shifting the radiation wavelength to higher values than the ZPL, alike a Stokes process in Raman scattering. In return a shift to higher energies as in anti-Stokes processes is also possible [9].

### 2.1.3. Optical Properties of NV Ensembles

In our experiments we used NV ensembles instead of single NVs, which behave differently from those. Advantageous for us was the better signal to noise ratio through the overall higher photon collection. Since the desired properties of the centre all belong to  $NV^-$ , a good  $NV^-$  to  $NV^0$  ratio is desirable. A spectrum of a NV ensemble is shown in figure 2.2(b), with both ZPLs present. For achieving good  $NV^-$  to  $NV^0$  contrast in measurements it is necessary to filter out the short wavelengths of the spectrum, as emission there belongs mostly to  $NV^0$ .

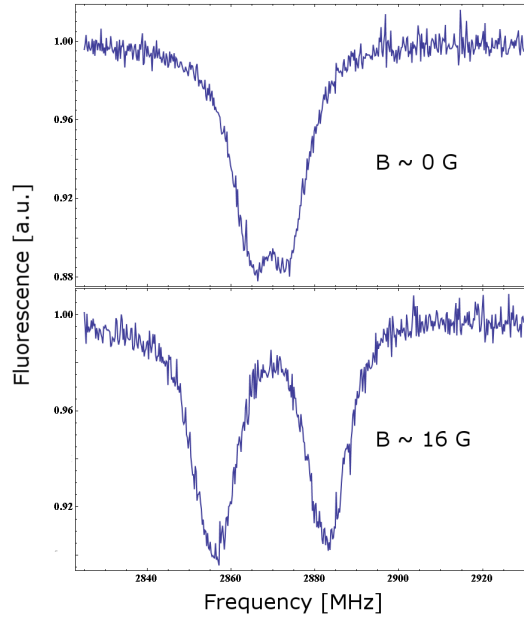


**Figure 2.3.:** Room temperature ground state ODMR spectra of NV ensemble without external magnetic field (above) and with magnetic field of 16G in [100]-direction (below).

## 2.2. Optically Detected Magnetic Resonance Measurements

The NV<sup>-</sup> fluorescence yield is strongly correlated with the lifetime and decay channels of its spin state. This feature is used in optically detected magnetic resonance (ODMR) measurements. This physical property of the NV centre can be used to perform magnetometry measurements.

The principle of ODMR measurements is described on the basis of the NV<sup>-</sup> ground state ODMR: On illumination with light of at least the ZPL energy, the NV<sup>-</sup> centre spins become optically polarized mainly in the  $m_s = 0$  ground state due to the different probabilities for the excited state decay paths as shown in figure 2.1(b). The  $m_s = \pm 1$  excited states likely decay into the singlet level  $^1A_1$  and following that into the long lived state  $^1E_1$ . They arrive finally from there with 70% in the

$m_s = 0$  state. By applying a microwave signal and scanning it over the ZFS region one derives an ODMR spectrum by looking at differences in the fluorescence yield while driving the  $m_s = 0$  to  $m_s = \pm 1$  ground state transition during illumination. At the resonance frequency, the fluorescence drops as a consequence of the refilling of the  $m_s = \pm 1$  states which after excitation show less fluorescence in decay than the  $m_s = 0$  state [12]. An ODMR spectrum is shown in figure 2.3, for both the excited and the ground state.

### 2.2.1. Zero-Field and Zeeman Splitting

The effective spin Hamiltonian for the ground state in terms of zero-field and Zeeman splitting is as follows [9]:

$$\begin{aligned}
 H_g &= H_{ZFS} + H_{Zeeman} \\
 &= D \left[ S_z^2 - \frac{1}{3} S(S+1) \right] + E(S_x^2 + S_y^2) + \mu_B g_e \vec{S} \cdot \vec{B}, \quad (2.1)
 \end{aligned}$$

with  $\hbar = 1$ ,  $S$  the electron spin operator, the fine structure splitting constant  $D$  and the strain induced splitting  $E$  with  $D = 2.87$  GHz and  $E \approx 0$  without strain,  $\mu_B$  is Bohr's magneton,  $g_e$  the g-factor and  $\vec{B}$  the magnetic field. In zero magnetic field, the magnetic dipole transitions of the NV are symmetric around  $D$ , while in an external magnetic field they become Zeeman shifted according to the effective field in the NV coordinate system.

## 3. Collection Optics Optimisation

As mentioned before, the first part of my thesis consisted of optics simulations and optimisation. First I want to describe the idea for the experimental setup behind the simulation model in section 3.1. Also, the proposed kinds of lenses are introduced there. To motivate the use of a collimating optic in more detail I am then going to discuss how efficient the experimental setup would be in theory without a collection optic. In section 3.2 the simulation results and drawn conclusions are presented. The chosen type of lens from the simulations had the potential for further improvement. By means of a Monte Carlo algorithm an enhanced lens was derived, as discussed in section 3.3.

### 3.1. Setup Outline

In the experiment we want to couple light emitted by a single NV directly into a fibre with high efficiency. Since the NV has a dipole radiation pattern and therefore emits with a large distribution of angles this is not an easy task. Furthermore, a significant amount of the light is reflected at the diamond surface decreasing the possible collection efficiency even further.

#### 3.1.1. Proposed Experimental Setup

We want to measure the fluorescence of the NVs with maximum efficiency. Since we are not interested in the imaging of the system but want to measure the overall

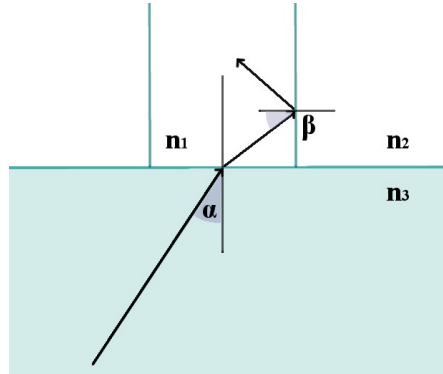


**Figure 3.1.:** *Illustration of the numerical aperture derivation (angles exaggerated).*

fluorescence output of the NVs, we do not require a microscopy setup as often used for NV fluorescence measurements. Further, we want a robust construction in terms of light coupling. In microscopy experiments, objective lenses have to be frequently readjusted to the right position. With that in mind our aim is to attach a fibre directly onto the diamond above the NV location with a collection optic in between, formed on the diamond surface. This lens will be fabricated by means of focused ion beam (FIB) milling. Such a setup can then be moved to different environments, for example a cryostat, more easily.

### 3.1.2. Coupling Efficiency without Lens

Below an estimate for the upper limit of the coupling efficiency without lens is derived.

We assume a NV centre is located  $2\ \mu\text{m}$  below the surface in a large bulk of diamond. It emits light and for the purpose here it is sufficient to assume that the radiation pattern is isotropic. First of all, the accepting angle of the fibre, which is located directly above the NV on the diamond surface and has a core diameter of  $4\ \mu\text{m}$ , is calculated by looking at the angle of total internal reflection. According

to Snell's law the critical angle for total internal reflection is given by

$$\beta = \arcsin\left(\frac{n_2}{n_1}\right). \quad (3.1)$$

With the refractive index of the fibre core of  $n_1 = 1.5$  and the refractive index of the fibre cladding of  $n_2 = 1.489$ ,  $\beta = 1.45$  rad, which is about  $83.1^\circ$ . All light that hits the fibre cladding with a smaller angle cannot be coupled into the fibre core. With another use of Snell's law refraction at the diamond surface is taken into account as illustrated in figure 3.1. The angle  $\gamma$  shall be  $\pi/2 - \beta$ , then

$$\sin(\gamma)n_1 = \sin(\alpha)n_3, \quad (3.2)$$

with  $n_3$  the refractive index of the diamond, so that

$$\cos(\beta)\frac{n_1}{n_3} = \sin(\alpha) \quad (3.3)$$

or

$$\sqrt{(1 - \sin(\beta)^2)} \cdot \frac{n_1}{n_3} = \sin(\alpha). \quad (3.4)$$

Inserting the total internal reflection condition for  $\beta$  leads to

$$\sqrt{1 - \left(\frac{n_2}{n_1}\right)^2} \cdot \frac{n_1}{n_3} = \sqrt{(n_1^2 - n_2^2)} \cdot \frac{1}{n_3} = \sin(\alpha). \quad (3.5)$$

The overall accepting angle is therefore  $\alpha = 0.043$  rad with  $n_3 = 2.4$ . Equation 3.5 is called the numerical aperture (NA) of a fibre or in general for an optical element.

In the next step I want to compute the ratio of a sphere segment that contains all the accepting angles of the fibre, and the area of the sphere. Since the angle for the integration is only 0.043 rad, the diameter of the fibre core is not the limiting factor for the light coupling.

$$dA_{sphere} = r^2 \sin\theta d\varphi,$$

$$A_{segment} = \int_0^{0.043} \int_0^{2\pi} r^2 \sin\theta d\varphi d\theta = 0.00092 \cdot 2\pi r^2.$$

Then the ratio is

$$\frac{A_{segment}}{A_{total}} = \frac{0.00092 \cdot 2\pi r^2}{4\pi r^2} = \frac{0.00092}{2} = 0.00046.$$

Since the accepted fluorescence light only has a small spread of angles we can assume vertical incidence onto the diamond to fibre interface and calculate the portion of light reflection  $R$  with [14]

$$R(\alpha = 0) = \left( \frac{n_3 - n_1}{n_1 + n_3} \right)^2 = 5.3\%. \quad (3.6)$$

Summing everything up, only about 0.044% of the light is coupled into the fibre. To improve this small value a lens is required.

### 3.1.3. Proposed Collection Optics

Since different kinds of lenses were compared in the simulations one of them, the Fresnel lens, is looked on briefly in this section before introducing the lenses compared in the simulations.

#### Fresnel Lenses

In the simulations one kind of simulated lenses were Fresnel lenses. These lenses are similar to Fresnel zone plates, therefore the plates are introduced here before discussing the lens further.

Fresnel zone plates consist of a substrate which has non-transparent rings on the surface that block the light contributing for either all the even or odd Fresnel zones to prevent destructive interference and to focus the light. The radius of the Fresnel zones depends on the focal length  $r_0$  and the wavelength of the light  $\lambda$  in the medium. The radius of the  $n^{th}$ -zone behaves as

$$\begin{aligned}
r_n &= \sqrt{(r^2 - r_0^2)} \\
&= \sqrt{\left(r_0 + n\frac{\lambda}{2}\right)^2 - r_0^2} \\
&= \sqrt{\left(nr_0\lambda + n^2\frac{\lambda^2}{4}\right)},
\end{aligned} \tag{3.7}$$

so that the path difference for adjacent zones is  $\frac{\lambda}{2}$ .

Fresnel lenses consist of rings etched into a substrate surface, with the radii of the rings behaving according to (3.7). Here, the light from neighbouring rings is not blocked but phase shifted to achieve constructive interference. The required phase shift of  $\frac{\lambda}{2}$  is determined through the difference in the optical paths, with the rings having height  $h$ ,

$$\frac{\lambda}{2} = (n_2 - n_1) h. \tag{3.8}$$

Therefore, we achieve the advantage that almost all the light contributes by constructive interference and it is focused onto a spot [14].

## Proposed Lenses

Two different kinds of collection optics were taken into account in the simulations. The first kind was a parabolic shape of the form

$$f(x) = -0.495868x^2, -2.2 \leq x \leq 2.2,$$

which we knew that we were able to produce with the FIB at that time. The other kind consisted of three different Fresnel lenses, two of them were derived by means of a genetic algorithm. The third one was derived as discussed in section 3.1.3 and is called 'binary' lens from this point. Fresnel lenses were assumed to be easier to

fabricate because less diamond material is needed to be milled off in creating them compared to the parabolic shape. All four lenses are shown as 3D plots and in cross-section in figure 3.2. The two Fresnel lenses derived by algorithm had small intermediate steps with the same step height of 88.47 nm, but one had four steps and the other only two.

## **3.2. Comsol Multiphysics Simulations**

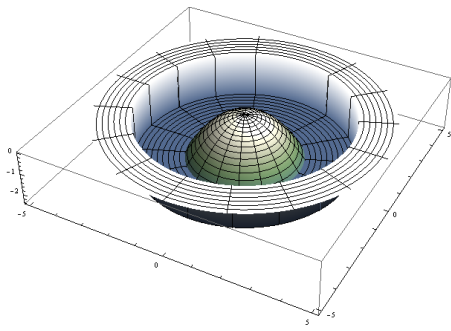
All simulations were conducted with the software 'Comsol Multiphysics' from this point on referred to as 'Comsol'. Some important features of the software are discussed in the following subsection, afterwards the optics simulations and their results are presented.

### **3.2.1. Comsol Multiphysics Software**

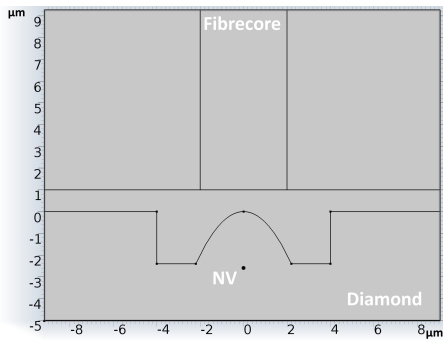
Comsol is a software for simulation of various kinds of physical problems. It uses a finite element method for solving partial differential equations. It has a graphical user interface for direct modelling and solving and is able to run on cluster computers. In the simulations Comsol version 4.3a was employed. Since the simulations were of an optical nature and hence frequency dependent, they were performed using the radio frequency (RF) module with a frequency domain study in two dimensions. Unfortunately, they could not be performed in three dimensions as this would have exceeded the available computing resources.

#### **Radio Frequency (RF) Module**

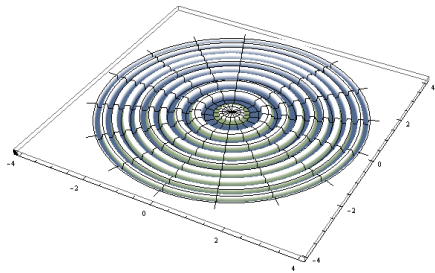
The RF module is capable of modelling electromagnetic wave propagation, transmission and reflection as well as dissipation in different materials. The solutions are derived from Maxwell's equations and material laws together with initial values and boundary conditions [15]. Of great importance was the possibility to use



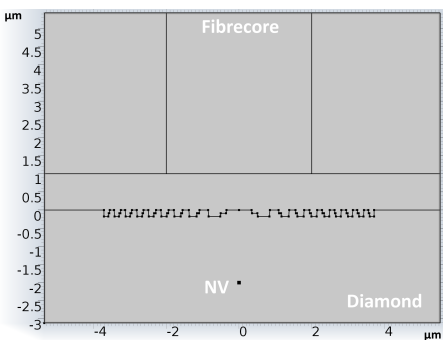
(a)



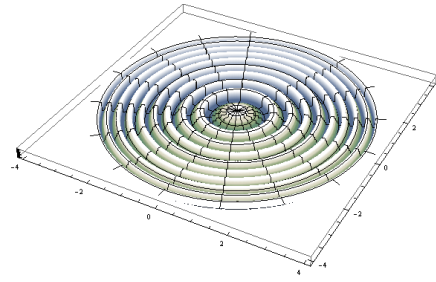
(c)



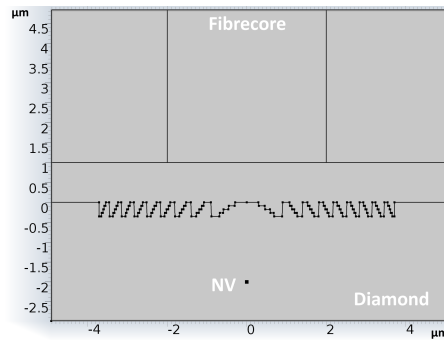
(e)



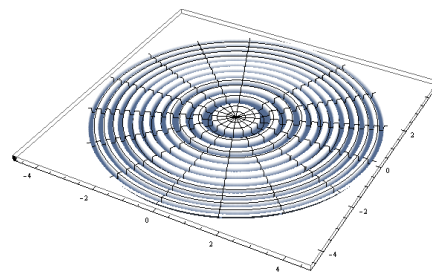
(g)



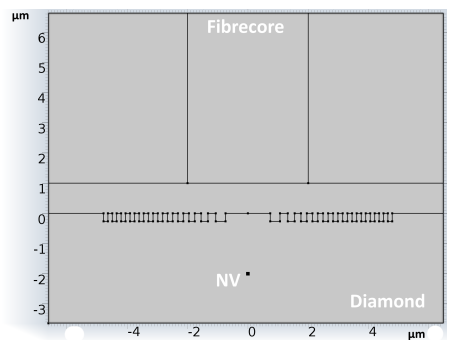
(b)



(d)



(f)



(h)

**Figure 3.2.:** Lens shapes plotted in 3D and cross-sectional: parabolic shaped lens, lens with four intermediate steps and lens with two intermediate steps and binary lens. All units in  $\mu\text{m}$ .

point sources, namely electric point dipoles, for simulating the emission pattern of single NVs.

### **Finite Element Solving**

Comsol solves estimates for the partial differential equations along a geometry mesh. Therefore the physical model is meshed into small elements before solving and if nothing else is specified it uses a triangular mesh with a set maximum mesh element size [15]. In the simulations discussed in the following the maximum mesh element length of the triangles was set to  $0.04\ \mu\text{m}$ . A second kind of mesh was used to reduce the number of mesh elements to decrease the computation time. This so called mapped mesh had a rectangular form where both lateral lengths can be specified and where the larger one was set to  $0.06\ \mu\text{m}$ .

### **3.2.2. Comsol Simulation Setup**

In the following a description of how the simulations were conducted and how the derived values for the lenses were compared is given. All simulations were carried out using Comsol with a two-dimensional setup. Optics simulations in 3D were not possible due to the huge size of the mesh that would have been necessary. The 2D values derived for the efficiencies could be compared for the lenses, but absolute values could not be taken from the simulations. I tested three different features of each lens: the overall best efficiency when aligned ideally and the sensitivity when the NV is either shifted horizontally or vertically in respect to the lens position. In the following the model used in the simulations is discussed in detail.

The simplified simulation model consisted of a NV in a bulk diamond located some micrometers below the surface. Directly above, as shown in figure 3.3, the core of a single mode fibre with four micrometers in diameter is aligned. For all simulations the fibre was always positioned centred above the lens. Surrounding the core is the fibre cladding, which will have a diameter of  $125\ \mu\text{m}$  in reality but it was not

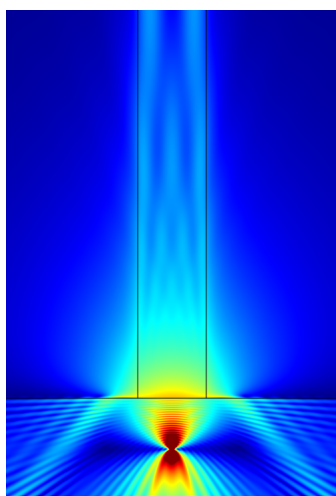


**Figure 3.3.:** *Simple schematic of the setup with radiating point dipole in diamond below a fibre core. The small angle of total internal reflection is discernible.*

necessary to account for the entire core in the simulations. Summing up, there were three different material domains in the simulations, characterised by their respective refractive indices - a diamond domain with a refractive index of 2.4, a fibre core with a refractive index of 1.5 and the fibre cladding with a refractive index of 1.48875. In the tests for the simulations I found out that it was necessary to add a small imaginary part of 0.01 to the refractive index of the cladding to remove some non-physical reflections that appeared in the cladding domain due to the geometry of the final simulation model.

Additionally, a so called *perfectly matched layer* (PML) was wrapped around the whole simulation model. This layer minimises reflections from the edges of the simulation domain. This measure also eliminated non-physical reflections from the borders of the simulation model. Neither the PML nor the imaginary part added to the refractive index could achieve the reflection elimination alone, so both had to be put into the simulation model. Since we required that the emission of the point dipole be coupled to a guided mode in the fibre, the model had to be quite long. 200  $\mu\text{m}$  were necessary for a Gaussian electric field to develop in the fibre core. The decrease in the Gaussian distribution due to the imaginary part

added to the cladding was accounted for in the final results. The field decay was determined to be exponential, and the exponent was found by targeted simulations. The unphysical loss could therefore be removed from the final values.

The final simulation model used is shown in figure 3.4. In the figure the PML domain is discernible as a small  $1\ \mu\text{m}$  wide border surrounding the whole model. All the material domains were the same as shown in the basic scheme of the setup. At the bottom of the model the diamond domain accommodates the point dipole and directly above it the tip of the fibre core domain surrounded by the two cladding domains is located. In the left inlay, the two different kinds of meshes used are shown. In the lower part of the model a finer triangular mesh was taken with maximum mesh element size of  $0.04\ \mu\text{m}$ , in the upper part a more coarse mapped mesh was used to reduce computation time.

All efficiency values were derived by integration of the time averaged power flow through the horizontal line at  $200\ \mu\text{m}$  and comparing this to the total time averaged power output of the dipole. Without any lens the coupling efficiency in this 2D simulation was 3.30% of the emitted power, assuming the dipole sits three  $\mu\text{m}$  below the fibre core. The lenses were later inserted in the diamond surface leading to a small gap between lens and fibre. In the experiment this gap will be a glue with refractive index of 1.5 to fix the fibre at the lens position and it was assumed to have a thickness of  $1\ \mu\text{m}$ .

The sensitivity of the system with respect to deviations of the lens-dipole alignment was tested by running parametric sweeps in Comsol. The simulation was then conducted for different vertical and horizontal positions of the point dipole relative to the lens. The simulations were performed with different dipole moment orientations. For this work the current dipole moment direction of (1,0) is the most important and will be discussed.

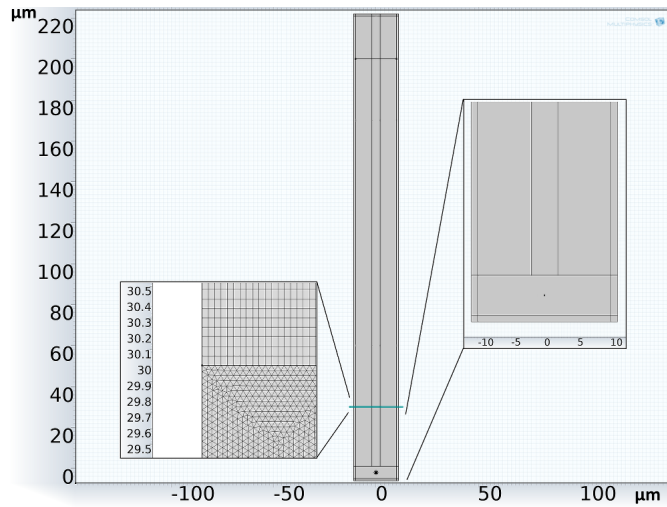


**Figure 3.4.:** *Final simulation model - the emitting point dipole is located in the lower part of the model, discernible as point in the right inlay. The left inlay shows the two different kinds of meshes used. For calculating the efficiency values of the lenses the time averaged power flow through the horizontal line at 200  $\mu\text{m}$  was looked at.*

### 3.2.3. Simulation Results and Conclusions

In this chapter, the simulation results are summed up and drawn conclusions are presented. All efficiency values are given for two dimensions.

#### Parabolic Lens

The first simulation run done with the parabolic lens was for the point dipole at different vertical positions below the centre of the lens in order to find out about the highest possible performance. The best efficiency was found between 3.4  $\mu\text{m}$  and 3.8  $\mu\text{m}$  below the surface of the diamond, with the highest value for efficiency of 25.91 % at 3.6  $\mu\text{m}$  (see figure 3.5(a)). All the obtained values for the vertical sweep are summed up in figure 3.5(d). Subsequently, at 3.6  $\mu\text{m}$  depth the lateral sweep of the dipole position was conducted. As shown in figure 3.5(c) already at 0.2  $\mu\text{m}$  deviation from the centred position the beam shape is altered strongly.

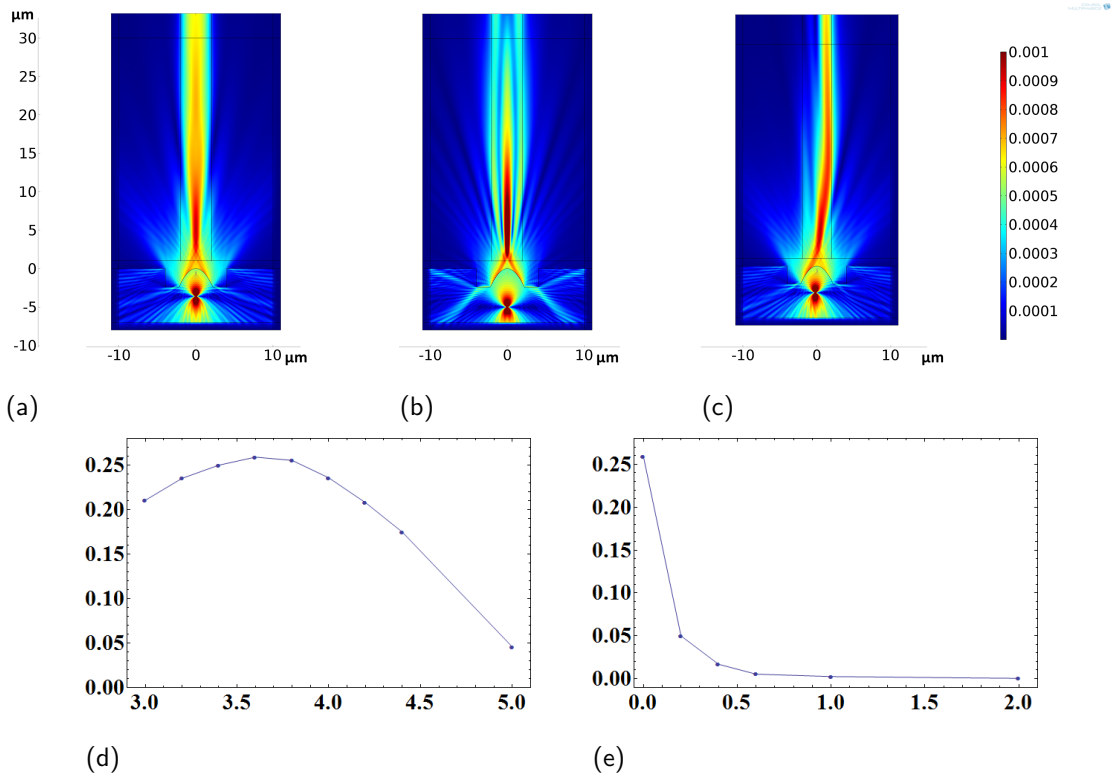


**Figure 3.5.:** Simulation results for the parabolic shaped lens: (a)–(c) electric field norm (V/m) surface plots: (a) dipole at the position with highest derived efficiency 3.6  $\mu\text{m}$  below the diamond surface, (b) dipole at a depth of 5  $\mu\text{m}$  below the diamond surface and (c) dipole shifted 0.2  $\mu\text{m}$  horizontally. (d) coupling efficiencies in the vertical sweep vs.  $\mu\text{m}$  depth and (e) coupling efficiencies in the horizontal sweep vs.  $\mu\text{m}$  deviation from centred.

This naturally has consequences for the efficiency values of this sweep direction, which are summed up in figure 3.5(e). At 0.2  $\mu\text{m}$  offset the performance left was only 4.99%. In a nutshell, the coupling decreases drastically already for small sideways shifts whereas the vertical stability is not that sensitive.

## **Fresnel Lenses with intermediate Steps**

The two Fresnel lenses with intermediate steps behaved quite similarly, therefore they are now presented together. Best efficiencies in the vertical sweeps were for both at a depth between  $1.8\ \mu\text{m}$  and  $2.2\ \mu\text{m}$ , as shown in figure 3.6(d), which was the depth they were designed for. Values for the lens with two steps were worse than the one with four steps throughout the whole sweep. The highest performance was 20.48% for the four step lens at  $2.0\ \mu\text{m}$  depth (figure 3.6(a)). In the horizontal sweeps, depicted in figure 3.6(b) and figure 3.6(c), both lenses had about equal performance with fast decreasing efficiencies. The results of the lateral sweep are summed up in figure 3.6(e).

## **Binary Fresnel Lenses**

Although the binary lens was designed also for an ideal dipole depth of  $2.0\ \mu\text{m}$ , highest performance in the vertical sweep was reached between  $2.2\ \mu\text{m}$  and  $2.6\ \mu\text{m}$  with the best derived efficiency value in the simulation of 15.21% at  $2.4\ \mu\text{m}$  (figure 3.7(d)). There are some factors which explain this behaviour: to derive the lens profile the simplified approach from section 3.1.3 was used, which works better when the focal length is large compared to the wavelength. Our focal length is in contrast quite short. The step height is large in relation to the focal length too, therefore more reflections take place at the step borders. And finally, we do not derive a Gaussian shape with the calculated lens.

In the horizontal sweep the efficiency decreased about equally fast as for the other lenses (figure 3.7(e)). Figures 3.7(a)–(c) illustrate some dipole positions.

## **Simulation Conclusions**

The most important values from the simulations are presented in table 3.1. The simulations showed that compared to the other lenses the parabolic shaped lens had the best performance in the sweeps. Therefore we decided to investigate such

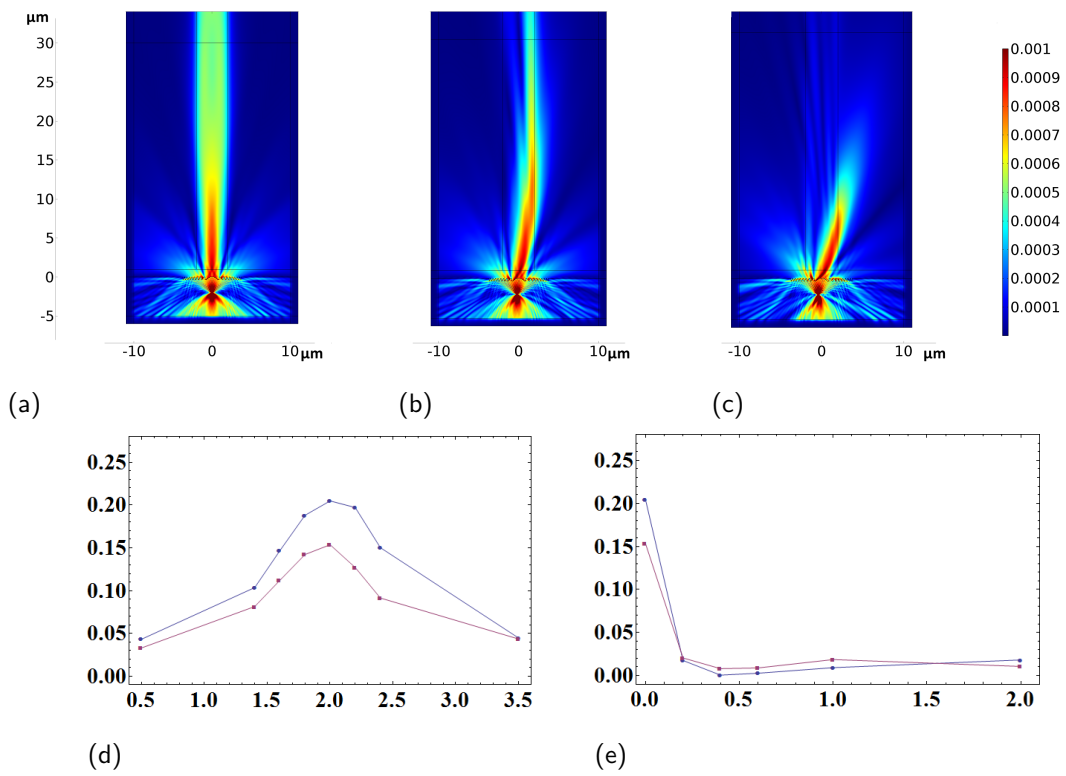


**Figure 3.6.:** Simulation results for the two Fresnel lenses with intermediate steps: (a)–(c) electric field norm (V/m) surface plots for Fresnel lens with four intermediate steps: (a) dipole at the position with highest derived efficiency  $2\ \mu\text{m}$  below the diamond surface, (b) dipole shifted  $0.2\ \mu\text{m}$  and (c)  $0.4\ \mu\text{m}$  horizontally. (d) coupling efficiencies in the vertical sweep vs.  $\mu\text{m}$  depth (blue - lens with four intermediate steps, red - lens with two intermediate steps) and (e) coupling efficiencies in the horizontal sweep vs.  $\mu\text{m}$  deviation from centred (blue - lens with four intermediate steps, red - lens with two intermediate steps).

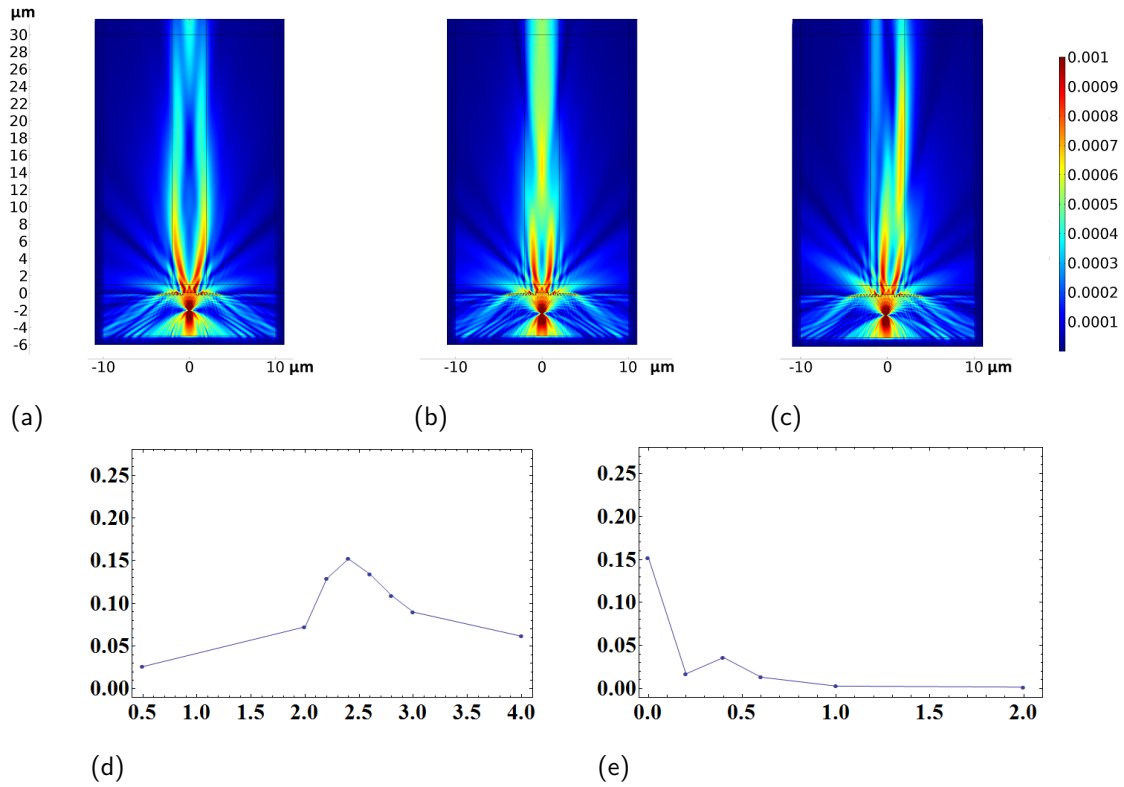


**Figure 3.7.:** Simulation results for the binary Fresnel lens: (a)–(c) electric field norm (V/m) surface plots: (a) dipole at design depth of 2  $\mu\text{m}$  below the diamond surface, (b) dipole at depth of 2.4  $\mu\text{m}$  with highest efficiency and (c) dipole shifted 0.2  $\mu\text{m}$  horizontally. (d) coupling efficiencies in the vertical sweep vs.  $\mu\text{m}$  depth and (e) coupling efficiencies in the horizontal sweep vs.  $\mu\text{m}$  deviation from centred.

Lens	Highest Efficiency	Efficiency 0.2 $\mu\text{m}$ from Centre
Parabolic Lens	25.91%	4.99%
Lens with 4 Int. Steps	20.48%	1.75%
Lens with 2 Int. Steps	15.36%	2.05%
Binary Lens	15.21%	1.71%

**Table 3.1.:** *Important lens efficiencies summed up for two dimensions.*

a lens further and optimise it. 25.91% efficiency means that still a large part of the light is lost when assuming that about 50% of the light can be potentially reached from one side. A drawback of the parabolic lens is the long fabrication time, since much material has to be milled off. If the milling process proves to be too slow a Fresnel lens is still a second option to keep since far less material has to be taken away in the fabrication. Again, it has to be pointed out that all efficiency values in this section are 2D estimates, therefore they will most likely be lower in 3D.

### 3.3. Collection Optics Optimisation

Now that we knew we wanted some parabolic or spherical shape it was the next step to improve the collection optics for our needs in the experiment. For this task we wrote a program which uses a Monte Carlo optimisation. The derived lens was then tested in further Comsol simulations.

#### 3.3.1. Optimisation Program

Below the program structure is outlined, but before that we introduce the geometric optics used in the algorithm.

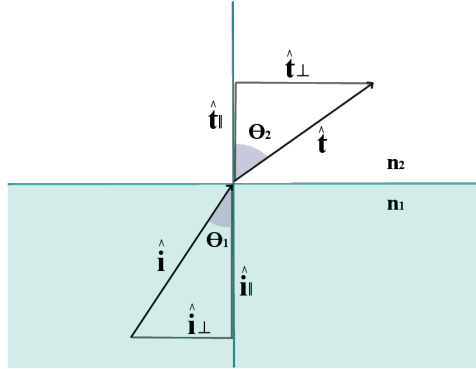


**Figure 3.8.:** *Refraction at the diamond surface with separation of incidence and transmitted unit vectors into parallel and perpendicular parts.*

### Refraction - Direction of Transmitted Light Ray

A ray of light travelling from the inside of a diamond to its surface is refracted according to Snell's law. The involved unit ray vectors of the incidence and transmitted beams can be separated into a parallel and a perpendicular part to the surface normal as shown in figure 3.8. We now want to express the direction of the transmitted vector  $t$  in terms of the refractive indices ( $n_1$  refractive index of diamond,  $n_2$  refractive index of glue), the angle of incidence  $\theta_1$ , the incidence vector  $i$  and the normal vector  $n$ .

$$\hat{t} = \hat{t}_\perp + \hat{t}_\parallel, \quad (3.9)$$

$$\hat{i} = \hat{i}_\perp + \hat{i}_\parallel. \quad (3.10)$$

With Snell's law one derives:

$$n_1 \sin \theta_1 = n_1 \frac{|\hat{i}_\parallel|}{|\hat{i}|} = n_2 \sin \theta_2 = n_2 \frac{|\hat{t}_\parallel|}{|\hat{t}|}, \quad (3.11)$$

so that

$$|\hat{t}_{\parallel}| = \frac{n_1}{n_2} |\hat{i}_{\parallel}|, \quad (3.12)$$

and therefore

$$\hat{t}_{\parallel} = \frac{n_1}{n_2} \hat{i}_{\parallel}. \quad (3.13)$$

With some vector analysis we express the parallel part of the incidence vector as

$$\hat{i}_{\parallel} = \hat{i} - (\hat{i}\hat{n})\hat{n} = \hat{i} - \cos\theta_1\hat{n}, \quad (3.14)$$

where  $\hat{n}$  is the unit normal vector to the diamond surface. By inserting equation (3.14) into equation (3.13) we have an expression for  $\hat{t}_{\parallel}$ . Further,  $\hat{t}_{\perp}$  can be expressed as

$$\hat{t}_{\perp} = \sqrt{|\hat{t}|^2 - |\hat{t}_{\parallel}|^2}\hat{n} = \sqrt{1 - |\hat{t}_{\parallel}|^2}\hat{n} = \sqrt{1 - \sin^2\theta_2}\hat{n}. \quad (3.15)$$

Inserting equation (3.13), (3.14) and (3.15) into equation (3.9) yields an expression for the unit transmitted vector  $\hat{t}$  as

$$\hat{t} = \frac{n_1}{n_2}\hat{i} - \left(\frac{n_1}{n_2}\cos\theta_1 - \sqrt{1 - \sin^2\theta_2}\right)\hat{n}. \quad (3.16)$$

Finally we eliminate the angle  $\theta_2$  from the expression using Snell's law.

$$\hat{t} = \frac{n_1}{n_2}\hat{i} - \left(\frac{n_1}{n_2}\cos\theta_1 - \sqrt{1 - \left(\frac{n_1}{n_2}\right)^2\sin^2\theta_1}\right)\hat{n}. \quad (3.17)$$

## Program Algorithm

The program written in C++ shapes a lens in iterative steps and each step includes one optimisation run. The Monte Carlo approach was chosen, rather than a raster sweep, due to its ability to create rapidly converging results without placing strong constraints on the input interval. A schematic of the theoretical model behind the program structure is shown in figure 3.9 and the source code is included in appendix A. A point emitter, marked as a red dot in the picture, is assumed to be

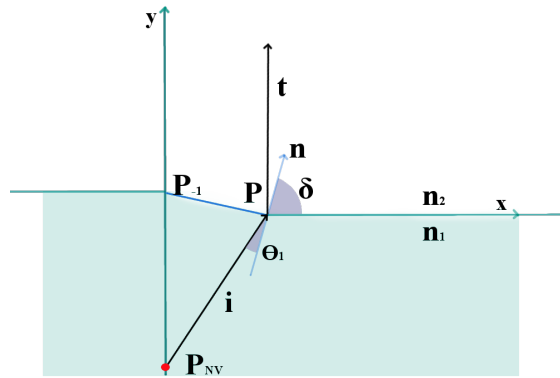


**Figure 3.9.:** Visualization of the calculation model of the program for the first lens surface element (blue line):  $i$  incidence vector,  $t$  transmitted vector,  $n$  normal unit vector to the lens surface element,  $\theta_1$  angle of incidence,  $n_1$  refractive index of diamond,  $n_2$  refractive index of glue,  $\delta$  random angle drawn,  $P$  intersection point of current lens surface element with current  $x$ -value,  $P_{-1}$  same as before for the last iteration run and  $P_{NV}$  location of the NV.

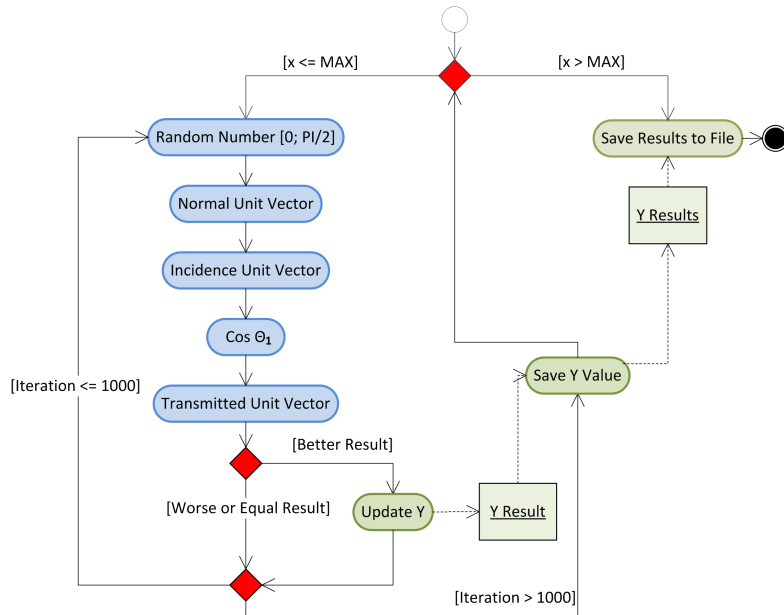


**Figure 3.10.:** Program flowchart: the algorithm starts at the white circle, entering then the first loop over the  $x$ -values. Subsequently, when  $x$  is smaller than the specified maximum value, the second loop with 1000 iterations is entered and a random angle is drawn. If it matches the optimisation target better than all iterations before, the corresponding  $y$ -value for the lens surface element is kept and after finishing the loop, saved to an array, that is written to a file on terminating the program.

located at a certain position  $P_{NV} = (x = 0, y = d)$  below the diamond surface with  $d$  the depth. Since the lens is assumed to be symmetric in  $x$ , the iteration process starts centred at  $x = 0$  and moves in a loop in positive  $x$ -direction in an  $x$ -increment size of choice. For each  $x$ -value a corresponding  $y$ -value is calculated, yielding an array of points which approximate the lens shape when the  $x$ -increments are sufficiently small. The optimisation target for each  $y$ -value calculation is that the direction of the transmitted ray is as close to the positive  $y$ -direction as possible.

In figure 3.10 the program flow is outlined. In the first step, the actual  $x$ -value is updated and when the value is smaller than the maximum  $x$ -value the loop on the left side is entered. A random angle  $\delta$  between 0 and  $\frac{\pi}{2}$  is chosen, which defines the tilt of the new lens element, since it is the angle between the  $x$ -axis and the lens element normal as shown in figure 3.9. Subsequently, the normal unit vector is derived with

$$\hat{n}_x = \cos\delta, \quad (3.18)$$

$$\hat{n}_y = \sin\delta. \quad (3.19)$$

Thereafter the incidence unit vector is obtained by looking at the point  $P$  where the current lens surface element intersects the current  $x$ -value so that

$$\hat{i} = \frac{\overline{P - P_{NV}}}{|P - P_{NV}|}, \quad (3.20)$$

with

$$P = P_{-1} + \begin{pmatrix} \Delta x \\ -\frac{\Delta x}{\tan\delta} \end{pmatrix}, \quad (3.21)$$

where  $P_{-1}$  is the intersection point from the last iteration and  $\Delta x$  the  $x$ -increment. From that  $\theta_1$  is calculated with  $\cos\theta_1 = \hat{n} \cdot \hat{i}$ . Now the transmitted unit vector can be derived according to equation (3.17). If it matches the optimisation condition better than all the other  $\delta$ -values before, the corresponding  $y$ -value is saved. When the loop is terminated, in this example after 1000 runs, the  $y$ -value is saved in an array and after finishing the  $x$ -loop the array is written to a file.

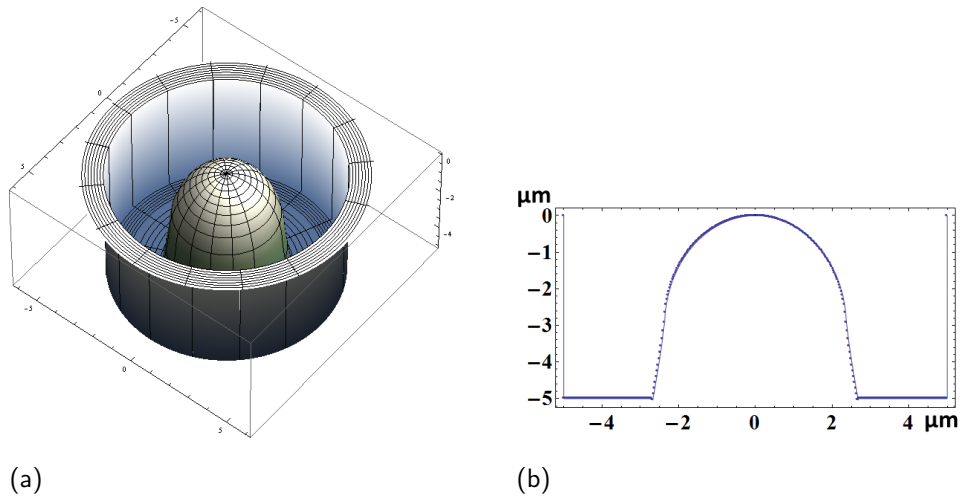


**Figure 3.11.:** *Derived lens from program as 3D and cross-sectional plots.*

### 3.3.2. Derived Lens

With an  $x$ -increment size of  $0.025 \mu\text{m}$  and maximum  $x$ -value of  $5.0 \mu\text{m}$  for a NV depth of  $5 \mu\text{m}$  the output lens is shown in figure 3.11. To compare the performance of this lens with the other lenses, I inserted the lens in the simulation model and ran it under the same settings as in chapter 3.2. The lens showed a 2D efficiency of  $30.26\%$  at  $P_{NV} = (0, -5)$  which is  $4.3\%$  more than the parabolic shaped lens had in the simulations. Colour plots of the lens performance are shown in figure 3.12(a)–(d). The results from the vertical and the horizontal shifts are shown in figure 3.12(e)–(f). Vertical stability was about equal to the parabolic shaped lens but the values were throughout higher. The same holds for the horizontal sweep, where at a shift of  $0.2 \mu\text{m}$  the efficiency was still  $6.36\%$ , which is  $1.37\%$  more than the parabolic shaped lens achieved.

### 3.3.3. Outlook

Since the simulations were conducted in two dimensions the 3D efficiency of the lens derived from the program is going to be much smaller, but will still be a large improvement compared to the case without lens. The remaining challenge is to

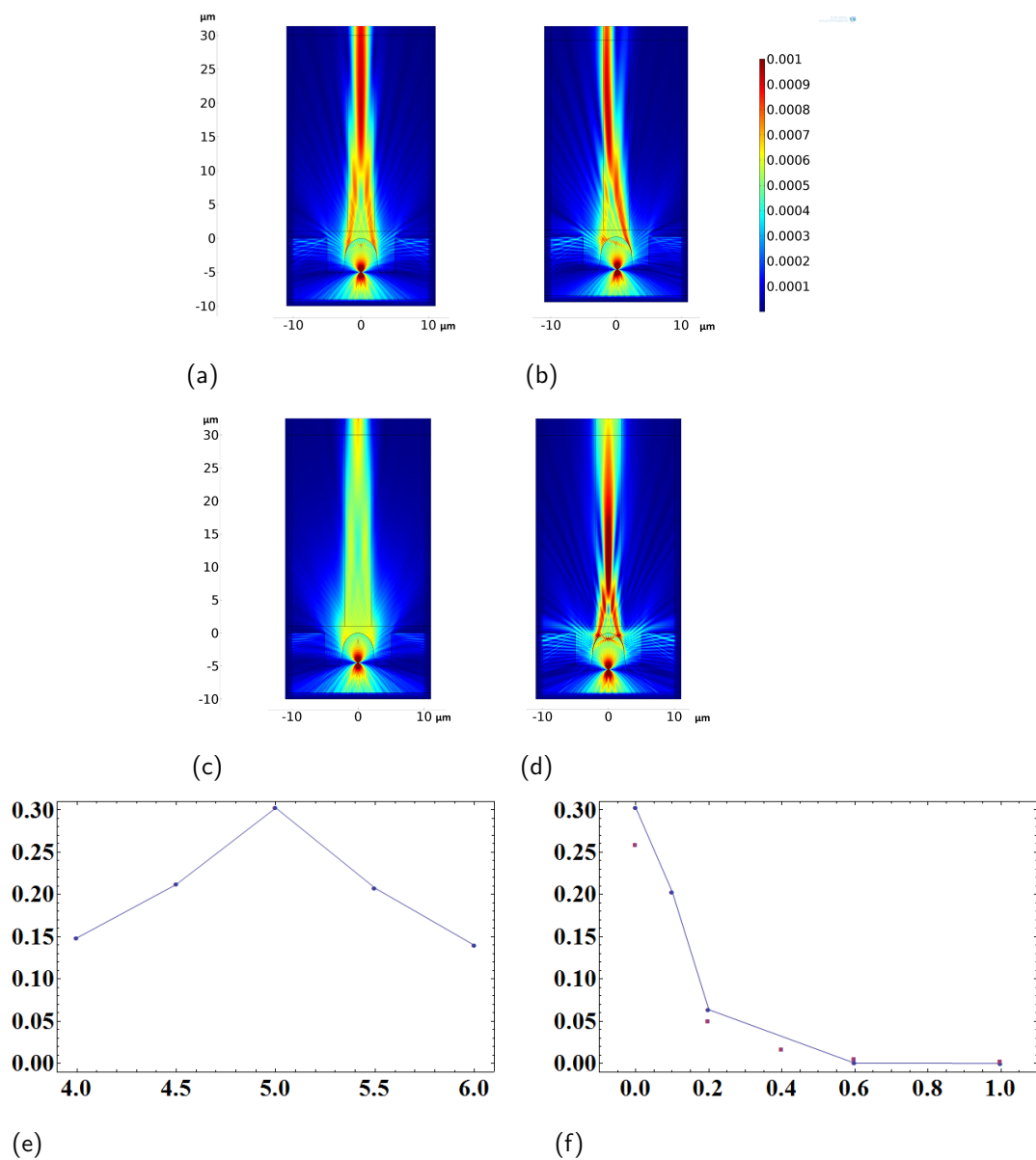


**Figure 3.12.:** Simulation results for the program derived lens: (a)–(d) electric field norm (V/m) surface plots: (a) dipole at position  $P_{NV}$ , (b) dipole shifted  $0.2 \mu\text{m}$  horizontally; (c) dipole shifted  $0.5 \mu\text{m}$  upwards and (d) dipole shifted  $0.5 \mu\text{m}$  away from the diamond surface. (e) efficiencies in the vertical dipole sweep, (f) efficiencies in the horizontal dipole sweep (blue line - lens from program, red dots - parabolic shaped lens).

construct such a lens at the site of a NV. After being able to achieve that there is still room for even more improvement of the lens or possibly also the trench around the lens. At the moment the program runs take only some seconds so that need of improving calculation speed is small but also easy to achieve by choosing the random angle  $\delta$  in the iteration runs from a reduced interval.

# 4. Direct Fibre Coupling of NV Ensembles

This chapter is focused on the assembly of a setup for directly fibre coupling ensemble NVs. The setup was tested through ODMR and magnetometry measurements. An advanced setup was developed after first measurements which is going to be introduced too. In the first section 4.1 the design, all the components used and construction of the experimental apparatus is described in detail. The optical properties of the setups and the collection efficiency are discussed. Subsequently, in section 4.2 some ODMR measurements performed on the setup are illuminated. Drawn conclusions and the experimental outlook are discussed in chapter 5.

## 4.1. Experimental Apparatus

Often, NV experiments are performed by means of a confocal microscope [16, 17]. We used a different approach for our experimental setup, which we constructed from scratch. Following up the experimental setup from chapter 3, we assembled the fibres for illumination with laser light and collection of fluorescence directly onto the diamond, so that readjusting the position of an objective lens as in confocal microscopy was not required and to transfer the construction to other environments can be done more easily. In the following, a detailed description of the experimental apparatus and employed components is given.

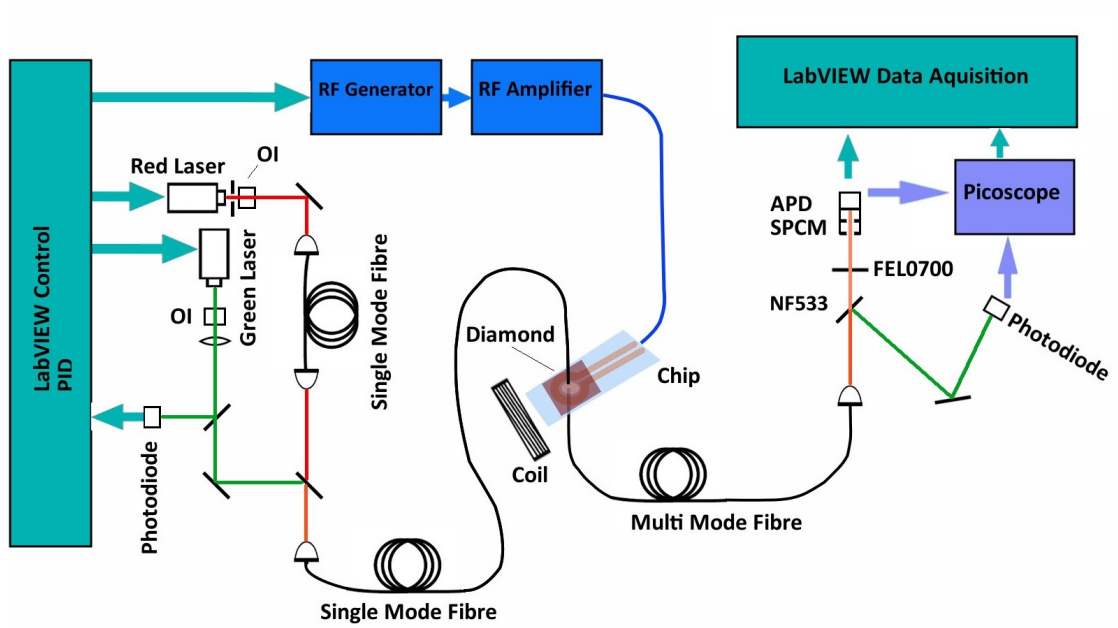
### 4.1.1. Setup Design

Since we wanted to conduct ODMR experiments we required for our setup, apart from the diamond, lasers for excitation, an optical system, a radio-frequency (RF) system and a method for data acquisition. To measure the magnetic field dependence of the NV ground state fine structure we also installed coils. After construction of a first setup, we were able to advance it for our requirements and constructed a second more effective assembly showing better stability. Schematic illustrations of the two different setups used are shown in figure 4.1. In the assembly, a diamond was glued onto a chip with a RF system and a small hole so that the laser light could pass through. On the left side of the figures the two lasers are shown, a green one and a red one, providing excitation light for the experiments. They were both coupled into a single mode fibre which was utilized for both setups as excitation path but in different ways. In the first setup built (figure 4.1(a)), the single mode fibre was glued directly onto the diamond. The light traversed the diamond and was collected by a multi mode fibre glued to the other side of the diamond through the small hole in the chip. In the second setup (figure 4.1(b)), developed after the experiments on the first setup, the laser light from the single mode fibre was coupled into the multi mode fibre and this fibre was used to illuminate the diamond and to collect the fluorescence light. In both cases the fluorescence light was, after leaving the multi mode fibre, filtered and then detected by a photodiode.

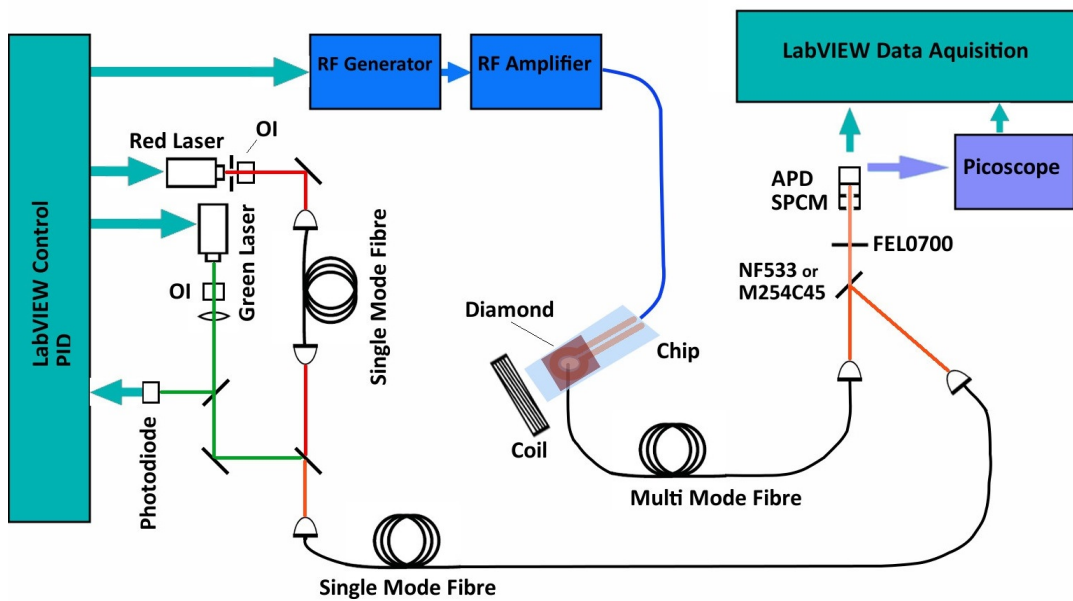
### 4.1.2. Lasers and Optical System

Two different lasers were in use for the experiments:

- a diode laser (Thorlabs DJ532-40) having a wavelength of 532 nm and 40 mW output power with housing built-in temperature stabilization. The beam was sent through an optical isolator and a lens with focal length of 150 mm. This laser showed very good long term stability when operated with a PID controller. Instead of a hardware controller we used a software version written



(a)



(b)

**Figure 4.1.:** The two different setups constructed, differing mostly in the path of the excitation light.

in 'LabVIEW' (National Instruments). At a glass plate a small fraction of the beam was fed to a photodiode for the PID feedback loop. The laser output was then controlled through LabVIEW.

- The second diode laser was a Thorlabs HL63133DG ( $\lambda = 637\text{ nm}$ ) diode with output power of 170 mW. It was temperature stabilized to 18 °C with a Thorlabs TED200C temperature controller and operated through LabVIEW with a Thorlabs LDC205C laser diode driver. After the diode an optical isolator was placed and then the beam was passed through a single mode fibre. A glass plate split off a small fraction of the beam which could be used for monitoring the laser with a photodiode.

Both laser beams were joined at a dichroic mirror (DMLP567, Thorlabs), which allowed the red light to pass but reflected the green light from the incidence path into the path of the red beam to couple them together into a single mode fibre.

The illumination path after the single mode fibre changed between setups. As shown in figure 4.1(a) for the first installation, the single mode fibre was directly used to illuminate the diamond and in the course of construction glued onto the diamond. The light then traversed a diamond mounted on a chip having a small hole to let the light pass through. Subsequently, the illumination light and the fluorescence light was collected below the diamond by a multi mode fibre and passed on to the detection system.

In the second setup, shown in figure 4.1(b), the light was first coupled to the multi mode fibre, which was also glued directly onto the diamond and additionally to illumination also provided the path for fluorescence collection.

The single mode fibre was of type SM450 (Thorlabs) and the multi mode fibre was a graded index fibre of type GIF625 (Thorlabs) with a core diameter of 62.5  $\mu\text{m}$ .

### 4.1.3. Theoretical Collection Efficiencies

Before discussing the assembly of the setups further, a closer look is taken upon the optical systems of both constructions in the diamond vicinity.

#### Light Transmission

In the first setup, the illumination light left the single mode fibre as Gaussian beam with a mode field diameter<sup>1</sup>  $\omega_0$  of about  $3.4\ \mu\text{m}$ . The light then travelled through a small layer of glue with the same refractive index as the fibre core. On entering the diamond the beam is assumed to diverge but keeps the Gaussian shape. The beam divergence angle  $\theta$  is defined as [18]

$$\theta = \frac{\lambda}{n\pi\omega_0}, \quad (4.1)$$

with  $\lambda$  the wavelength of the light and  $n$  the refractive index of the medium. For  $\lambda = 532\ \text{nm}$  the divergence angle in diamond with a refractive index of 2.4 is  $0.0208\ \text{rad}$ . This angle defines a cone shaped volume in the diamond where NV centres undergo excitation as shown in figure 4.2. As the diamond had a thickness of  $300\ \mu\text{m}$  the mode field diameter increases to  $15.88\ \mu\text{m}$  on the other side, where a multi mode fibre with a core diameter of  $62.5\ \mu\text{m}$  is glued to. Therefore, in theory with ideal alignment, all the light passing the diamond and which is not reflected on entering the fibre could be coupled to the multi mode fibre. The initial light intensity from the single mode fibre nevertheless decreases through reflection at both diamond surfaces according to equation (3.6) and due to scattering and absorption in the diamond. The reflections would account for 5.3% loss of intensity on each surface.

---

<sup>1</sup>Diameter where maximum intensity decreased to  $\frac{1}{e^2}$

## Fluorescence Collection

Light with wavelength smaller than the ZPL can be absorbed by the NV centres in the diamond, subsequently leading to fluorescence. Assuming the NVs have a uniform density  $\rho$  throughout the diamond and a wavelength dependent absorption cross section  $\sigma(\lambda)$ , the number of absorbed photons  $dN$  per length interval  $dx$  behaves as

$$\frac{dN}{dx} = -N\rho\sigma(\lambda), \quad (4.2)$$

with the number of incidence photons  $N$ . By counting the fluorescence photons the product of absorption cross section and NV density can be estimated. Another approach, which is taken for this thesis, consists in comparing fluorescence rates of NVs with published values. For that it is crucial to know about the fraction of the fluorescence that can be collected with the multi mode fibre. Then the overall fluorescence can be derived and from that our fluorescence collection efficiency and the total photon absorption in the diamond.

Multi mode fibres are able to collect all the light that has an incidence angle within the numerical aperture (NA), which we derived as

$$\sin(\alpha) = \frac{1}{n_3} \sqrt{n_1^2 - n_2^2}, \quad (4.3)$$

in equation 3.5 with  $\alpha$  the half angle of incidence,  $n_3$  the refractive index of the material outside the fibre,  $n_1$  the refractive index of the fibre core and  $n_2$  the refractive index of the fibre cladding [14]. The multi mode fibre had a NA for a medium with  $n_3 = 1$  of 0.275 according to the manufacturer, leading to a NA for diamond of  $0.275/2.4 = 0.115$ . Some light from outside the cone defined by the angle  $\alpha$  is also coupled into the fibre but not very effectively and therefore neglected. With a height of  $270.5 \mu\text{m}$  the cone does not reach through the whole diamond. This situation is depicted in figure 4.2.

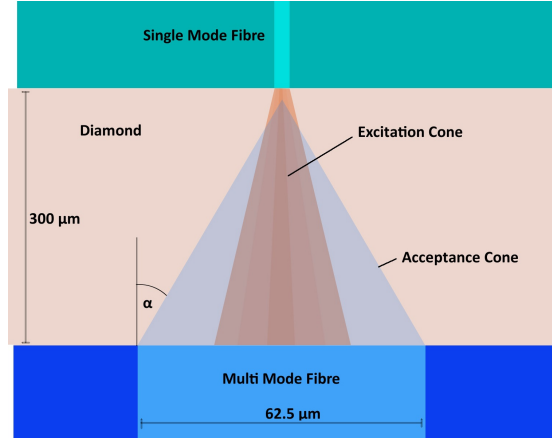


**Figure 4.2.:** Fluorescence collection in the first setup illustrated schematically. The excitation cone has a Gaussian distribution of intensity.

In the next step, the fluorescence collection efficiency of this fibre setup is estimated. From figure 4.2 we can see that most of the fluorescence light emitted within the NA angle is collected by the multi mode fibre, only in the upper part some more of the fluorescence is lost. But even from above the acceptance cone some light is collected with a maximum acceptance angle smaller than the NA angle. Therefore, it is assumed that all the fluorescence light of the NVs which is emitted in direction of the multi mode fibre within a maximum angle of the NA angle can potentially be gathered. This leads to the following expression for the collection efficiency when assuming an isotropic emission pattern of the NVs in all directions:

$$\begin{aligned}
 \eta &= \frac{1}{4\pi} \cdot \int_0^{2\pi} \int_0^\alpha \sin(\theta) d\theta d\varphi \\
 &= \frac{1}{2} (1 - \cos(\alpha)) = \sin^2\left(\frac{\alpha}{2}\right) = \sin^2\left(\frac{\sin^{-1}(NA)}{2}\right) \\
 &= 0.0033.
 \end{aligned} \tag{4.4}$$

With this integration over all the accepted angles of a sphere surrounding the NV we derive an overall collection efficiency  $\eta$  of only 0.33 % of the total fluorescence.

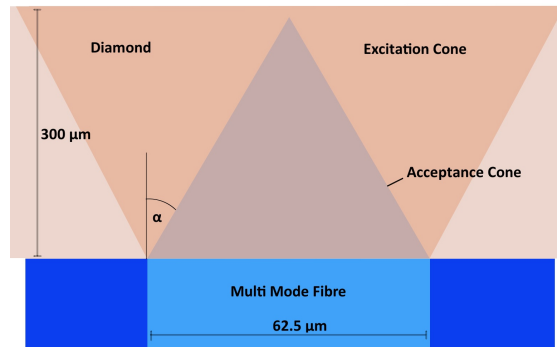


**Figure 4.3.:** *Fluorescence collection in the second setup illustrated schematically. The excitation cone has a continuous distribution of intensity.*

Though small, this collection efficiency is nonetheless eight times greater than that of a single-mode fibre, as calculated in section 3.1.2.

In the second setup, shown in figure 4.1(b), the collection efficiency is the same for the volume in the acceptance cone. The illumination light leaving the multi mode fibre had a divergence angle of the NA angle, as shown in figure 4.3. The intensity is assumed to be distributed evenly over the circular area of the fibre core when the light leaves the fibre. In this case, all the NVs in the acceptance cone are reached by the illumination. This marks the main difference between the setups. In the first setup, NVs are more easily saturated by the illumination light intensity than in the second setup, where illumination spreads out more evenly. Therefore, with higher intensities, the second setup will more likely show a higher fluorescence yield. Moreover, the difficulty of aligning the fibres exactly does not arise in the second setup.

#### **4.1.4. Diamond Properties**

In the experiments two different diamonds containing NV ensembles were examined. They were labelled 'Q5' and 'Q6'. Both diamonds were electron irradiated

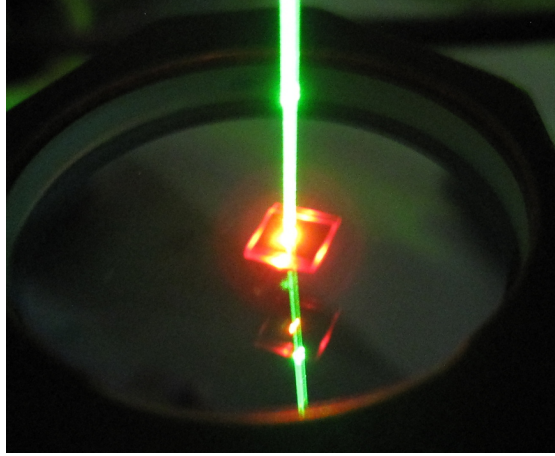


**Figure 4.4.:** *Diamond 'Q5' emitting fluorescence light on illumination with green laser through a single mode fibre glued to the surface.*

and subsequently annealed to form NV centres. In figure 4.4 the diamond Q5 is shown emitting fluorescence light when illuminated with a green laser. The dimensions of both diamonds were about 3.1 times 3.1 mm and 0.3 mm in height. The flat sides were polished on the [100]-surface of the crystal.

#### **4.1.5. RF System and Coils**

To generate the RF signal for the ODMR measurements we used a TTI TGR6000 RF signal generator, which had a frequency range from 10 MHz up to 6 GHz and allowed for fast frequency setting with the option to use USB remote control. The generated signal was fed into a high power amplifier of the type ZHL-16W-43-S+ (Mini-Circuits) with a gain of 45 dB. The amplifier was directly connected to the chip which harboured the diamond. On the chip but beneath the diamond an antenna structure was fabricated in the manner of a short, visible in figure 4.5(a). Frequency and amplitude of the RF signal were controlled via LabVIEW.

In the magnetic field dependency measurements of the NV fine structure, a pivotable coil was installed around the chip setup with a centre field of about 16 G at 4 A. It was provided with a DC current through a TTI QL564TP power supply,

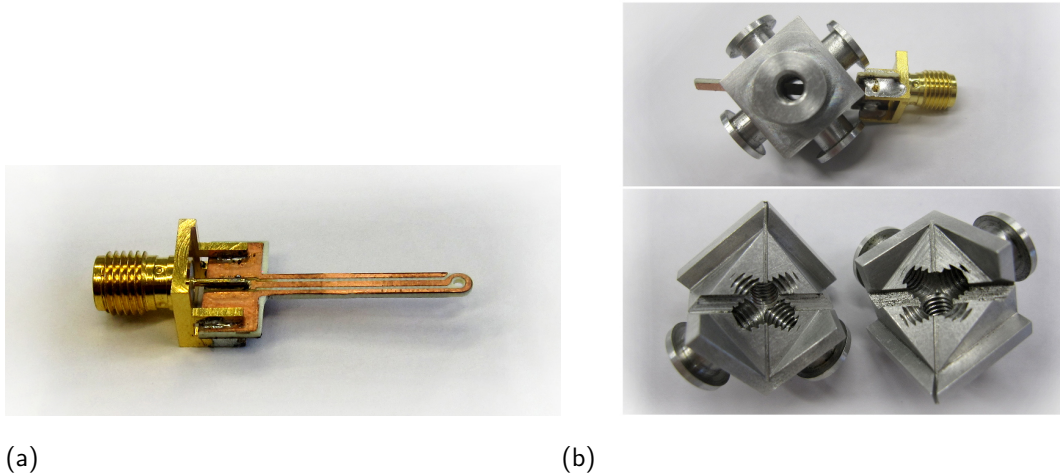


**Figure 4.5.:** (a): Chip with RF antenna at the tip; (b): the cube with chip inserted, consisting of two separate parts shown in the lower picture.

also controlled by the LabVIEW program. The coil was later on in the experiments replaced with an aluminium cube mount shown in figure 4.5(b). It consisted of two parts that perfectly fit together, leaving just enough room for the chip and the diamond in the horizontal slot and for the fibres in the two small vertical slots. On the outer side six attachments were placed for coils.

#### 4.1.6. Detection System and Data Acquisition

After leaving the multi mode fibre the fluorescence light could be detected in different ways. It was separated from possible green light with a notch filter (Thorlabs NF533), which reflects the green laser light. In the second setup this filter was used in the illumination path as a mirror for coupling the green excitation light into the multi mode fibre. The filter reflects light in a 17 nm region around the centre wavelength of 533 nm. After this filter, other filters and mirrors could be placed in the beam path. Of great importance was the Thorlabs FEL0700 long pass filter placed into the fluorescence light path before detection. It ensured that light with wavelength smaller than 700 nm was filtered out of the beam. This measure is required to block a part of the fluorescence light from  $NV^0$  in order to

promote NV<sup>-</sup> fluorescence detection since their spectra have less overlap above a wavelength of 700 nm.

Various types of diodes were used for detection of the fluorescence light or for laser monitoring:

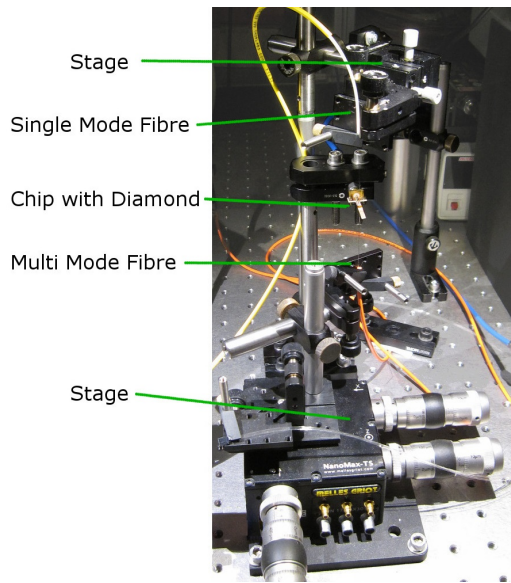
- A Thorlabs PDA36A amplified photodetector provided gain of the signal of up to 70 dB while having low noise.
- An avalanche photodetector of type APD110A (Thorlabs) was employed for small signals but showed noisy behaviour.
- When the fluorescence light was fibre coupled again, it could be analysed with a single photon counting module (Excelitas SPCM-AQRH-12-FC) or fed into an Ocean Optics Maya2000Pro spectrometer.

The diode signals were read out by a National Instruments card, or a 'Pico-Scope3404B' (Pico Technology) which delivered a less noisy signal. The data were then processed in LabVIEW programs and subsequently analysed, with the LabVIEW version 2010.

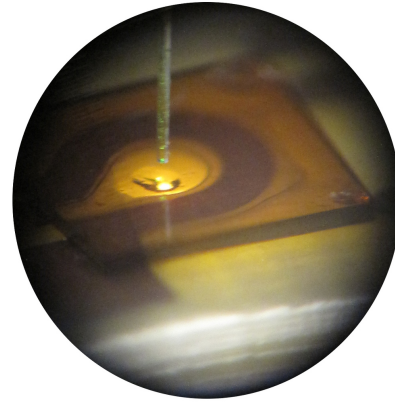
#### **4.1.7. Assembly Process**

The assembly process of the setups was done in separate steps since the gluing procedures of the fibres took two days for each part. It was required to use a glue with good transparency in the visible and infrared light range which cured at room temperature and would be suitable for a cryogenic environment. For these tasks we chose the two component epoxy EPO-TEK301 (Epoxy Technology), which cured in at least one day at room temperature and comprised all the mentioned features.

For fixation and achieving good stability during the assembly a stage was set up, which is shown in figure 4.6(a). It allowed to clamp the chip in a stable way and offered two position and tilt adjustable stages for the aligning and gluing process of the fibres. The fibres were prepared by removing the fibre cladding from the



(a)



(b)

**Figure 4.6.:** (a): the assembly stage with chip and aligned fibres, (b): vision through a magnifying glass onto the diamond after gluing of the multi mode fibre to the bottom side of the diamond.

tip, cleaning and cleaving. In the first gluing step, the diamond was put onto the antenna structure of the chip. Two days later, the multi mode fibre was glued to the bottom side of the diamond through the 1 mm hole in the chip. In figure 4.6(b) the already glued multi mode fibre can be made out as bright spot. The single mode fibre is aligned but not yet glued. To ensure good alignment of the fibres the transmission from the single mode to the multi mode fibre was monitored during the whole process. After curing, the single mode fibre was glued onto the top side of the diamond after realigning for maximum transmission. Upon completing some measurements the cube was set onto the assembly and glued as well as screwed together.

## 4.2. Optically Detected Magnetic Resonance Experiments

During assembly it was already possible to test the ODMR measurement setup. In the following the measurement scheme is presented and some experiments with green and red excitation light are introduced.

ODMR measurements in our setups always followed the same scheme: A list of frequency values and corresponding amplitudes was passed on from LabVIEW to the frequency generator. This was repeated twice in order to minimize frequency setting errors. The list had two amplitude values for each frequency, one with the actual set gain (often -7 dBm) and one with the lowest possible gain (-110 dBm), which equalled no microwave at the diamond at all. In short, the RF signal was switched on and off in one frequency step. When all frequencies were passed, the generator started setting the RF signal according to the list and fed those to the amplifier. Simultaneously, after receiving a trigger signal, the pico-scope started to measure the fluorescence signal from the avalanche photodiode with a sampling rate of  $2 \cdot 10^6$  per second. On finishing the frequency settings list the measured data were transferred from the pico-scope to the computer and evaluated in LabVIEW by computing the ratios in fluorescence values for consecutive periods with RF signal and periods without RF signal. Choosing this way of measurement proved to eliminate low-frequency fluctuations in the setup, for example mechanical vibrations.

### 4.2.1. Green Laser Illumination

The measurements presented in figure 4.7 were conducted on the first setup with diamond Q5 and the coil surrounding the setup, positioned in the same plane as the chip and the flat side of the diamond with the field in direction of the fibres. Different currents were applied varying from 0 to 4 A, corresponding up to about 16 G magnetic field strength at the diamond position. The Zeeman splitting of the

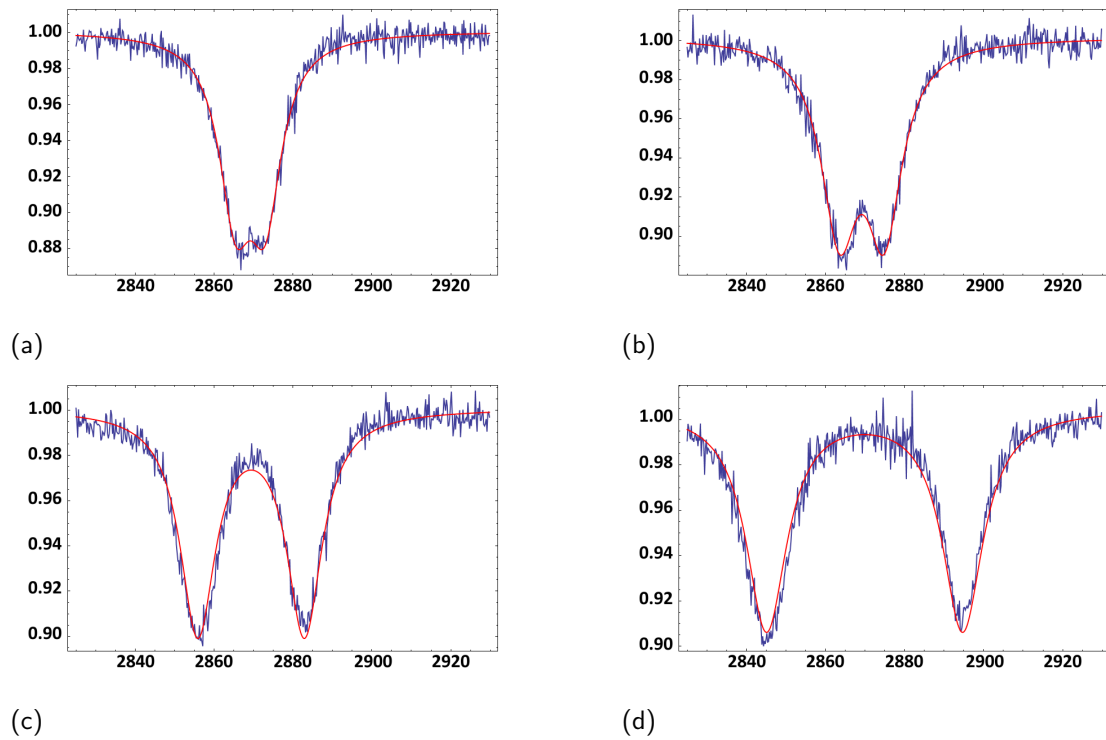


**Figure 4.7.:** (a)–(d) ODMR measurements at different coil currents and resulting magnetic fields in  $[100]$ -direction of the diamond crystal axis. Values on x-axis in MHz, y-axis in arbitrary units: (a) no current, (b) 2.5 G, (c) 8.4 G and (d) 16.3 G; with thanks to Georg Wachter.

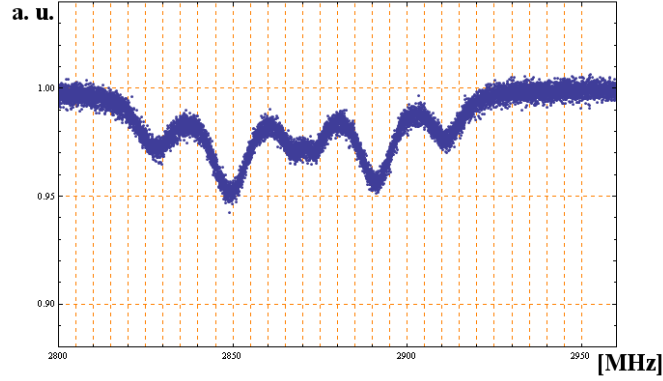


**Figure 4.8.:** ODMR with green excitation light and a coil tilt of about  $45^\circ$  to the diamond  $[100]$ -axis. NV families 'see' different magnetic field strengths and therefore show varying Zeeman splitting; with thanks to Georg Wachter.

$m_s = \pm 1$  states is pointed out in the figures for different field strengths. Fits (red lines) were obtained by the use of two Lorentzian functions:

$$f(x) = 1 - \frac{a_1}{1 + \frac{(x-x_0+w)^2}{g}} - \frac{a_1}{1 + \frac{(x-x_0-w)^2}{g}}, \quad (4.5)$$

where  $a_1$  is describing the amplitude of the peaks,  $x_0$  and  $w$  are defining the centre position of the peaks and  $g$  is a scaling parameter for the peak width. Contrast for the measurements was very good with about 10 to 12% and the dip positions were symmetrically aligned around the  $m_s = 0$  to  $m_s = \pm 1$  transition frequency of 2.87 GHz. Independent of the applied field strengths only two equally deep dips were visible at a time, as required by the symmetry of the system. Each dip was created by four dips of the overall eight dips from all the NV families in the diamond.

By tilting the coil with an angle of about  $45^\circ$  more than just two dips became visible, shown in figure 4.8. Due to the new system symmetry, NV families in the diamond experienced different magnetic field directions and strengths resulting in a more individual Zeeman splitting.

## 4.2.2. Red Laser Illumination

Differing from the experiments explained above we also excited the diamond solely with red laser light in the second setup with diamond Q6. We compared those measurements to the green illumination only case to investigate their difference in contrast.

As illumination path the mirror M254C45 was used instead of the notch filter NF533, to reflect the illumination light from the single mode fibre into the multi mode fibre as shown in figure 4.1(b). This mirror reflected nearly all the wavelengths smaller than 750 nm, including our red excitation laser, and transmitted greater wavelengths. The fluorescence was measured by the SPCM after passing the FEL0700 filter.

Contrast for the red excitation only ODMR was very good with about 11%, even though the fluorescence signal was small. The measurement is shown in figure 4.9(a), contrasted by a measurement with only green excitation in figure 4.9(b) with the same fluorescence counts per second outcome as in the red ODMR for comparison. The contrast for this measurement was lower with only about 9%. With green illumination some contrast is lost since not only  $NV^-$  is excited but also  $NV^0$ , which does not participate in the ODMR fluorescence cycle.

In order to investigate the ODMR-contrast behaviour more closely we measured and subsequently calculated the density of the NV centres in the diamond and the ratio between  $NV^-$  and  $NV^0$  to gain a better understanding of our sample and to compare those values to previous values by Nöbauer et. al. [9].

### NV Density Estimation

We estimated the density of NVs in the diamond and especially the density of  $NV^-$ . This was done by first estimating the density of all NVs and then looking at the ratio of  $NV^-$  to  $NV^0$ .

To estimate the NV density we measured the fluorescence yield of diamond Q6

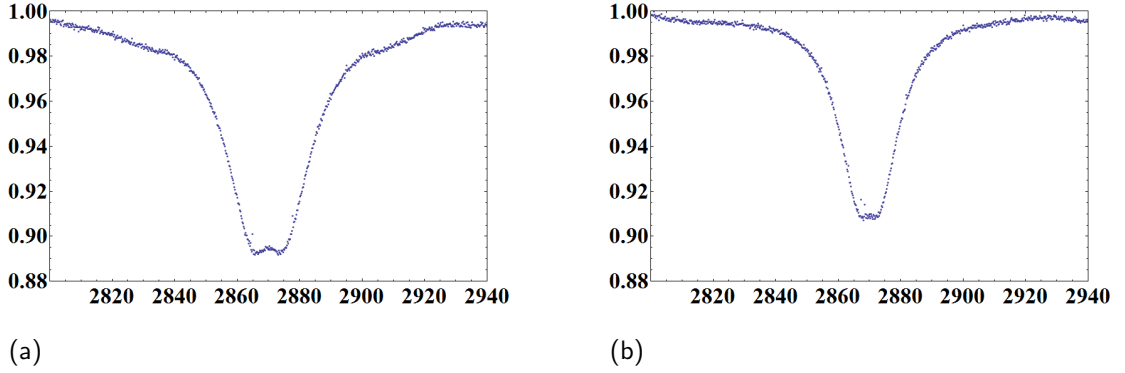


**Figure 4.9.:** (a): ODMR with only red excitation light showing good contrast, (b): ODMR with only green excitation light yielding lower contrast - at the same level of fluorescence output as in the red excitation ODMR. Values on x-axis in MHz, y-axis in arbitrary units.

under illumination with green light in the second setup. With green light both  $NV^-$  and  $NV^0$  are excited. A spectrum with green illumination for Q6 is shown in figure 4.11(a) and was measured with the Maya spectrometer. To derive the NV density we compared our fluorescence yield with the correlation for a single NV at room temperature between green laser excitation power and fluorescence behaviour derived by Kurtsiefer et al. [2].

Kurtsiefer et al. reported a detection efficiency of  $1.5 \cdot 10^{-4}$  for their confocal microscopy setup with spot size diameter in the diamond of  $0.43 \mu\text{m}$ . Assuming the single NV centre only 'sees' the maximum of the Gaussian distributed intensity profile of the excitation beam, the correlation between excitation power  $P$  and maximum intensity  $I_0$  behaves as

$$P = I_0 \cdot \int \int e^{-2 \frac{x^2 + y^2}{w^2}} dx dy = I_0 \cdot \frac{\pi}{2} w^2, \quad (4.6)$$

with beam waist  $w$  of  $0.215 \mu\text{m}$ . For our excitation power we were far below any saturation and could assume the linear behaviour in fluorescence counts reported by Kurtsiefer et al. for low powers, which we extrapolated as

$$R(P) = \frac{5085}{1.3} \cdot P = k \cdot P, \quad (4.7)$$

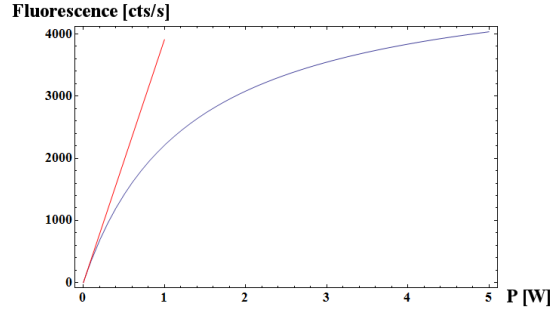


**Figure 4.10.:** Linear approximation for low powers (red curve) on saturation curve of a single NV (blue curve) taken from [2].

with  $R(P)$  the fluorescence counts depending on excitation power  $P$  in their setup (figure 4.10).

Therefore we can sum the total fluorescence for their single NV up as

$$R(P) = \frac{k \cdot P}{\eta_K} = \frac{k}{\eta_K} \cdot I_0 \cdot \frac{\pi}{2} w^2, \quad (4.8)$$

with  $\eta_K$  the detection efficiency. We now compare this expression with our fluorescence yield for  $n$  NV centres. For an illumination power of 8 mW at the diamond a total fluorescence power of 15  $\mu$ W was measured coming back through the multi mode fibre. Assuming all of them had a mean wavelength of 660 nm and hence the energy per photon of  $3 \times 10^{-19}$  J we had

$$\frac{15 \cdot 10^{-6}}{3 \cdot 10^{-19}} = 5 \cdot 10^{13} \quad (4.9)$$

photons per second, leading to the total rate of fluorescence per second  $R$  of

$$R = \frac{5 \cdot 10^{13}}{\eta} \quad (4.10)$$

The estimated collection efficiency  $\eta$  of our setup was the collection efficiency derived in section 4.1.3 times losses due to reflection at the diamond-glass interface as derived in equation 3.6:

$$\eta = 0.0033 \cdot 0.95. \quad (4.11)$$

Our ensemble fluorescence rate  $R$  is now compared to the fluorescence rate from the paper but for  $n$  NV centres, the number of NVs in the acceptance cone of the multi mode fibre. This leads to the expression

$$R = \frac{k}{\eta_K} \cdot I_0 \cdot \frac{\pi}{2} w^2 n. \quad (4.12)$$

The excitation intensity decreases for NVs further away from the multi mode fibre since the beam spreads out evenly on entering the diamond as discussed in section 4.1.3. The intensity in the diamond depends on the height  $h$  above the multi mode fibre by

$$I(h) = \frac{P}{A(h)_e} \quad (4.13)$$

with  $A(h)_e$  the area of the circle defined by the excitation cone at a certain height. Having a NV density of  $\varrho$  per cubic centimetre, the fluorescence of the ensemble per second is

$$R = \frac{k\eta}{\eta_K} \cdot \frac{\pi}{2} w^2 \int_0^{h_{max}} \frac{P}{A(h)_e} \varrho A(h)_a dh \quad (4.14)$$

with  $A(h)_a$  the radius of the acceptance cone at height  $h$  and  $h_{max}$  the height of the cone, then

$$= \frac{k\eta}{\eta_K} \cdot \frac{\pi}{2} w^2 P \varrho \int_0^{h_{max}} \frac{A(h)_a}{A(h)_e} dh \quad (4.15)$$

$$= \frac{k\eta}{\eta_K} \cdot \frac{\pi}{2} w^2 P \varrho \int_0^{h_{max}} \frac{\left(-\frac{r_{MM}}{h_{max}}h + r_{MM}\right)^2}{\left(\frac{r_{MM}}{h_{max}}h + r_{MM}\right)^2} dh \quad (4.16)$$

$$= \frac{k\eta}{\eta_K} \cdot \frac{\pi}{2} w^2 P \varrho \int_0^{h_{max}} \frac{(-h + h_{max})^2}{(h + h_{max})^2} dh \quad (4.17)$$

$$= \frac{k\eta}{\eta_K} \cdot \frac{\pi}{2} w^2 P \varrho \cdot (3h_{max} - 4h_{max} \ln(2)) \quad (4.18)$$

and therefore

$$5 \cdot 10^{13} = \varrho \cdot 0.000029 \Rightarrow \varrho = 1.72 \cdot 10^{18}. \quad (4.19)$$

One part per million (ppm) in diamond equals  $1.77 \cdot 10^{17}$  atoms per cubic centimetre. We derive for diamond Q6 9.71 ppm. Diamond Q5 is assumed to be quite similar to Q6 in NV concentration. Since we neglected losses in the fluorescence light detection path after the diamond, this result can be interpreted as a lower boundary for the NV density.

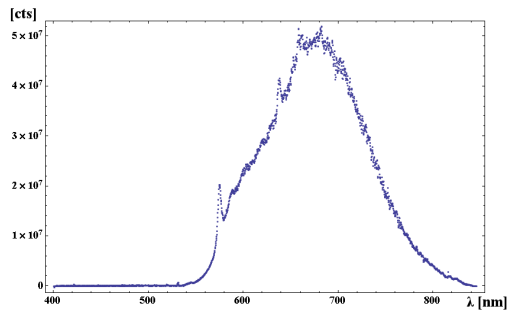
The ratio of  $NV^-$  and  $NV^0$  in the diamond was approximated with the fluorescence spectra of the two diamond samples. An approximation is possible by comparing the net areas of the ZPL peaks in the spectrum [19]. Spectra of both diamonds are shown in figure 4.11(a) and figure 4.11(b). As shown in figure 4.11(c) the phonon side-band background of diamond Q6 was interpolated with one linear function for each ZPL peak. This function was subtracted from the peak and the remaining counts were integrated. Calculating the ratio of  $NV^-$  to  $NV^0$  then yields 0.37, which corresponds to the concentration ratio by a factor of two [19], yielding a concentration ratio of 0.74. For diamond Q5 the ZPL ratio of  $NV^-$  to  $NV^0$  is 0.48 and the concentration ratio is therefore 0.96 (figure 4.11(d)).

By comparing the density value and the ratio of  $NV^-$  to  $NV^0$  to previous values by Nöbauer et. al. [9] we concluded that they are broadly consistent. We also concluded that we can rely on our collection efficiency derivation. With our NV concentration we had sufficient  $NV^-$  for good contrast in our ODMR experiments. Therefore we want to further improve the contrast by means of finding a good ratio in green and red laser excitation light.

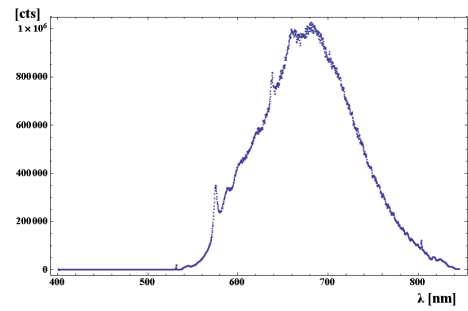
## **ODMR Contrast**

To improve the ODMR contrast we want to investigate the fluorescence behaviour of ensemble samples under illumination with a mixture of green and red excitation light in order to find an optimum.

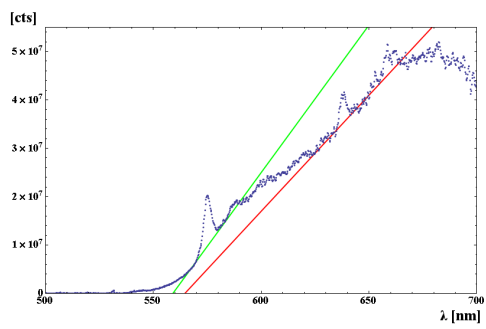
In the ODMR measurements with green excitation light after filtering the fluorescence we still had a contribution of  $NV^0$  to the background signal which decreased our contrast by 22%. Nevertheless, the fluorescence signal in this case is huge



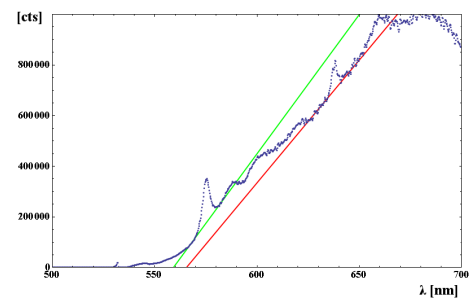
(a)



(b)



(c)



(d)

**Figure 4.11.:** (a):spectrum of fluorescence from diamond Q6 and (b) Q5 on illumination with green laser only; (c)–(d): illustration of  $NV^-$  to  $NV^0$  ratio calculation for (c) Q6 and (d) Q5.

compared to the ODMR measurements with only red excitation.

In the future, we want to find an optimum in our signal to noise ratio and contrast by mixing green and red laser excitation. We are going to use different filters to cut away less fluorescence signal. We could potentially use half of the spectrum of  $\text{NV}^-$  by only filtering out the red and green excitation light.

## 5. Conclusions and Outlook

In the course of this thesis we could get some steps closer to our goal of directly fibre coupled single NVs.

The main tasks in this thesis were the simulations of different collection optics for the decision which type of lens to choose for the experiment and to improve it subsequently. An assembly for direct fibre coupling was constructed and tested in different measurements leading to an advancement of the setup for our current purpose.

Drawn conclusions from the measurements, from the assembly and the simulations are summed up in this chapter and a future outlook for the ongoing experiments is given.

In the collection micro-optics simulations the software Comsol was employed to investigate four different lenses, a parabolic shaped one and three Fresnel lenses for their efficiency in the experiment. Unfortunately, the software only allowed for two-dimensional simulations so that we could compare the lenses to each other but we could not derive absolute values. Nevertheless, in the comparison we found the parabolic shape to perform best and decided on improving it further. However, the construction of this type of lens needs more time and effort than the Fresnel lenses, so that we may decide for a more easy to fabricate Fresnel type of lens in the future. The parabolic shape showed potential for improvement, which was done by a numerical optimisation. An iterative algorithm produced a lens shape through Monte Carlo optimisation. The derived lens revealed the highest efficiency to date in a simulation run. This lens is now being created in a cleanroom by the

use of FIB-milling.

Following this work an experimental apparatus was constructed from scratch for direct fibre coupling of ensemble NVs. Fibres were glued at their tips directly onto a diamond and provided excitation and fluorescence collection paths. The first setup constructed consisted of a single mode fibre and an aligned multi mode fibre. Once glued they did not require readjustment like for example objectives of confocal microscopes. In the course of assembly we developed precise and stable techniques for aligning and attaching the fibres for future application once a single NV with milled lens is ready. In ODMR measurements we could demonstrate microwave control and 3D control of the magnetic field.

The setup could then be adjusted for our current requirements, which consist in magnetometry measurements, stability tests and NV density estimation, by having only one multi mode fibre glued to the diamond and operating it as excitation and collection path. Through this measure we achieved excellent stability and alignment to another fibre was not necessary any more, allowing for even more accurate ODMR and subsequently magnetometry measurements. Furthermore, we were able to address more NV centres in the excitation and had more potential for fluorescence light collection, since saturation effects occur at higher incident power. Through the use of the multi mode fibre for excitation and collection we simplified the optical path which allowed us to estimate the NV density and concentration in the diamond more easily.

The next step in the experiment is going to be a test of the second setup, which was installed into a cube mount, under cryogenic conditions through ODMR measurements with different magnetic fields applied. We want to further develop an ODMR-based magnetometer as a practical and low cost device. As soon as the FIB-milled lens sitting above a single NV is ready we are going to assemble a similar setup as the first one presented in this thesis to directly fibre couple the single NV to a single mode fibre. We will use the NV centre in this setup as a qubit, as a single photon source and for further study of the physics of NV centres.

# A. Appendix

## A.1. Optimisation Program Source Code

```
1 #include <iostream>
2 #include <cmath>
3 #include <fstream>
4 #include <stdlib.h>
5 #include <time.h>
6 using namespace std;
7
8 float findY (float, float, float, float, float, int, float);
9
10 // y-value optimisation method
11 float findY (float xMax, float xNumber, float depth, int xCounter,
12             float yValuePlus)
13 {
14     float delta = 0.0; // Random Angle
15     float yValue = 0.0; // y-value in iteration
16     float yValueReturn = 0.0; // y-value to return from iteration
17     float normX = 0.0; // x-component of normal vector
18     float normY = 0.0; // y-component of normal vector
19     float incX = 0.0; // x-component of incidence vector
20     float incY = 0.0; // y-component of incidence vector
21     float costheta = 0.0; // incidence angle
22     float transX = 0.0; // x-component of transmitted vector
23     float transY = 0.0; // y-component of transmitted vector
24     float n1 = 2.4; // refractive index of diamond
25     float n2 = 1.5; // refractive index of fibre
```

```

26  int i = 0; // counter variable
27  const double PI = 3.141592653589793238462;
28  float check = -2; // optimisation condition check variable
29  float n = n1 / n2;
30
31  float xValue = xMax / xNumber * xCounter; // current x-value
32
33  if (xValue==0) yValueReturn = -depth; // check if on starting x-
    position
34  else
35  {
36      if (yValuePlus <= 0.0) yValueReturn = 0.0; // check if y is
        already at NV depth
37      else
38      {
39          for (i=0; i < 1000; i++) // optimisation loop
40          {
41              delta = (rand() % 1000)*(PI/2)/999); // random angle
42
43              // calculaton of norm vector components
44              normX = cos(delta);
45              normY = sin(delta);
46
47              // calculaton of incidence vector components
48              incX = (xValue)/(sqrt(pow(xValue,2)+pow(yValuePlus-((
                xMax/xNumber)/tan(delta)),2)));
49              incY = (yValuePlus-((xMax/xNumber)/tan(delta)))/(sqrt
                (pow(xValue,2)+pow(yValuePlus-((xMax/xNumber)/tan(
                delta)),2)));
50
51              // calculation of incidence vector
52              costheta = normX * incX + normY * incY;
53
54              // calculaton of transmitted vector components
55              transX = n*incX-(n*costheta-sqrt(1-(n*n*(1-costheta*
                costheta))))*normX;
56              transY = n*incY-(n*costheta-sqrt(1-(n*n*(1-costheta*
                costheta))))*normY;

```

```

57
58         // optimisation condition
59         if ((transY - 1) > (check))
60         {
61             check = transY - 1;
62             yValue = yValuePlus-(xMax/xNumber)/tan(delta);
63         }
64
65     }
66     if ((i >= 999) && (check > 0.1)) yValueReturn = 0.0;
67     else (yValueReturn = yValue);
68 }
69 }
70 return (yValueReturn);
71 }
72
73
74 int main ()
75 {
76     int xNumber=200; // number of x-values
77     float xMax=5; // highest x-value
78     float depth=-5.0; // depth of NV centre in diamond
79
80     float xValue=0.0; // current x-value
81     float yValuePlus = 0.0; // y-value from last iteration run
82     float points[xNumber+1][2]; // result array
83
84     srand (time(NULL));
85
86     points[0][0]=0.0;
87     points[0][1]=0.0;
88
89     // x-value loop
90     for ( int xCounter = 0; xCounter <= xNumber; xCounter++)
91     {
92         xValue=xMax/xNumber*xCounter;
93         float result = findY (xMax, xNumber, depth, xCounter,
94                             yValuePlus);

```

```
94
95     // record result in array
96     points[xCounter][0] = xValue;
97     points[xCounter][1] = result + depth;
98     yValuePlus = result;
99 }
100
101 return 0;
102 }
```

Listing A.1: Optimisation Program Source Code

# Bibliography

- [1] A. Gruber, A. Dräbenstedt, C. Tietz, L. Fleury, J. Wrachtrup, and C. Von Borczyskowski. Scanning confocal optical microscopy and magnetic resonance on single defect centers. *Science*, 276(5321):2012–2014, 1997.
- [2] C. Kurtsiefer, S. Mayer, P. Zarda, and H. Weinfurter. Stable solid-state source of single photons. *Physical Review Letters*, 85(2):290–293, 2000.
- [3] F. Jelezko, T. Gaebel, I. Popa, A. Gruber, and J. Wrachtrup. Observation of coherent oscillations in a single electron spin. *Physical review letters*, 92(7):076401, 2004.
- [4] L.P. McGuinness, Y. Yan, A. Stacey, D.A. Simpson, L.T. Hall, D. Maclaurin, S. Prawer, P. Mulvaney, J. Wrachtrup, and F. Caruso. Quantum measurement and orientation tracking of fluorescent nanodiamonds inside living cells. *Nature nanotechnology*, 6(6):358–363, 2011.
- [5] M.V. Gurudev Dutt, L. Childress, L. Jiang, E. Togan, J. Maze, F. Jelezko, A.S. Zibrov, P.R. Hemmer, and M.D. Lukin. Quantum register based on individual electronic and nuclear spin qubits in diamond. *Science*, 316(5829):1312–1316, 2007.
- [6] K. Nemoto, M. Trupke, S.J. Devitt, A.M. Stephens, K. Buczak, T. Nobauer, M.S. Everitt, J. Schmiedmayer, and W.J. Munro. Photonic architecture for scalable quantum information processing in nv-diamond. *arXiv preprint arXiv:1309.4277*, 2013.

- [7] A.M. Zaitsev. *Optical properties of diamond: a data handbook*. Springer, 2001.
- [8] F. Jelezko and J. Wrachtrup. Single defect centres in diamond: A review. *physica status solidi (a)*, 203(13):3207–3225, 2006.
- [9] Nöbauer, T. *Sensing, coherent coupling and optimal control with nitrogen-vacancy colour centres in diamond*. PhD thesis, Technischen Universität Wien, 2013.
- [10] N.B. Manson, J.P. Harrison, and M.J. Sellars. Nitrogen-vacancy center in diamond: Model of the electronic structure and associated dynamics. *Physical Review B*, 74(10):104303, 2006.
- [11] D.M. Toyli, C.D. Weis, G.D. Fuchs, T. Schenkel, and D.D. Awschalom. Chip-scale nanofabrication of single spins and spin arrays in diamond. *Nano letters*, 10(8):3168–3172, 2010.
- [12] M.W. Doherty, N.B. Manson, P. Delaney, F. Jelezko, J. Wrachtrup, L.C.L. Hollenberg. The nitrogen-vacancy colour centre in diamond. *Physics Reports*, 528:1–45, 2013.
- [13] V.M. Acosta, A. Jarmola, E. Bauch, and D. Budker. Optical properties of the nitrogen-vacancy singlet levels in diamond. *Physical Review B*, 82(20):201202, 2010.
- [14] Demtröder W. *Experimentalphysik 2*. Springer, 2006.
- [15] *COMSOL Multiphysics Reference Guide*, Version 4.3b.
- [16] G. Balasubramanian, I.Y. Chan, R. Kolesov, M. Al-Hmoud, J. Tisler, C. Shin, C. Kim, A. Wojcik, P.R. Hemmer, and A. Krueger. Nanoscale imaging magnetometry with diamond spins under ambient conditions. *Nature*, 455(7213):648–651, 2008.

- [17] J.R. Maze, P.L. Stanwix, J.S. Hodges, S. Hong, J.M. Taylor, P. Cappellaro, L. Jiang, M.V.G. Dutt, E. Togan, and A.S. Zibrov. Nanoscale magnetic sensing with an individual electronic spin in diamond. *Nature*, 455(7213): 644–647, 2008.
- [18] B.E.A. Saleh and M.C. Teich. *Fundamentals of Photonics*. John Wiley & Sons, 2007.
- [19] V.M. Acosta, E. Bauch, M.P. Ledbetter, C. Santori, K.-M.C. Fu, P.E. Barclay, R.G. Beausoleil, H. Linget, J.F. Roch, and F. Treussart. Diamonds with a high density of nitrogen-vacancy centers for magnetometry applications. *Physical Review B*, 80(11):115202, 2009.

# Acknowledgments

I enjoyed the work on this master's thesis a lot even though I had to rack my brain about many new topics, which provided a great opportunity to gain experience in for me beforehand unknown terrains. Of course, that would not have been possible without all the people in the group who I now want to acknowledge.

I am very grateful to Prof. Jörg Schmiedmayer for the chance to do this thesis in such a flourishing group with its enthusiastic atmosphere. My perception in that time was that especially young and motivated people are welcomed cordially and supported in their endeavours.

Special thanks go to my supervisor Michael Trupke, whom I got to know as extremely dedicated and professional researcher. I highly value his way to challenge me to do my best, supporting creative solutions while always giving the right amount of support and taking time for the concerns of his students.

Many thanks to my colleagues Fritz Ladinig and Georg Wachter for the great teamwork and the nice time while idle waiting for measurements. I want to thank the team I could be part of Kathrin Buczak, Christian Derntl, Cameron Salter and Rui Vasconcelos - it was a pleasure working with you. Thanks also to all the other people in the group.

I want to thank my family for the strong support during my studies and for backing me up morally as well as listening to my concerns.